Electrochimica Acta 506 (2024) 145010

Contents lists available at ScienceDirect

Electrochimica Acta

journal homepage: www.journals.elsevier.com/electrochimica-acta

# Material parameters affecting Li plating in Si/graphite composite electrodes

Lioba Boveleth [a,b], Adrian Lindner [c], Wolfgang Menesklou [c], Timo Danner [a,b,*], Arnulf Latz [a,b,d]

[a] German Aerospace Center, Institute of Engineering Thermodynamics, Pfaffenwaldring 38-40, Stuttgart, 70569, Germany
[b] Helmholtz Institute Ulm for Electrochemical Energy Storage, Helmholtzstraße 11, Ulm, 89081, Germany
[c] Karlsruhe Institute of Technology, Institute for Applied Materials – Electrochemical Technologies, Adenauerring 20b, Karlsruhe, 76131, Germany
[d] Ulm University, Institute of Electrochemistry, Albert-Einstein-Allee 47, Ulm, 89081, Germany

## ARTICLE INFO

*Keywords:*
Commercial lithium-ion battery
Silicon-graphite composite
3D microstructure-resolved simulation
Lithium plating
Competitive lithiation

## ABSTRACT

Silicon is a frequently used active material in the negative electrode of lithium-ion batteries which provides significant improvements in the energy density. Due to large volume changes during cycling, it is typically mixed with graphite. Understanding the interactions of composite materials during battery operation is key to optimizing battery performance and predicting aging phenomena. Even though lithium plating is a critical degradation process, which influences both lifetime and safety, a systematic analysis of electrochemical material parameters affecting plating in composite electrodes is missing. Therefore, a parameter study is performed using 3D microstructure-resolved simulations. We investigate the influence of critical material parameters such as open-circuit potential, electronic conductivity, chemical diffusion coefficient, and exchange current density in simple and interpretable model geometries. The simulations reveal the importance of chemical diffusion and exchange current density, as well as their ratio, in predicting plating. Finally, we apply the set of material parameters to a complex electrode geometry reconstructed from FIB/SEM tomography data of commercial anode material. The analysis shows that preferential plating on the electrode surface dominates all other factors.

## 1. Introduction

The global demand for high-performance batteries continues to grow. While the primary characteristics depend on the application, the key criteria are energy density, safety, cost, and sustainability of the batteries. Lithium-ion (Li-ion) batteries play a key role, especially for electric vehicles (EVs) and portable electronics. A popular option for the negative electrode material is still graphite due to its long cycle life, high abundance, and comparatively low cost [1,2]. However, further improvements are needed, for example, to achieve sufficient driving range. A promising material for the anode is silicon, which is both abundant and offers a ten times higher theoretical capacity (3579 mAh/g for $Li_{15}Si_4$) compared to graphite (372 mAh/g for $LiC_6$) [3,4]. Silicon, on the other hand, experiences large volume changes during lithiation and delithiation and generally has low Li mobility negatively impacting cycle life and performance [5,6]. To take advantage of the high theoretical capacity and limit deformation during cycling, Si is mixed with graphite in Si/graphite composite electrodes [7,8]. However, electrochemical aging mechanisms, especially Li plating, have not been extensively studied in the literature due to complex interactions between the different materials in the electrode microstructure.

Plating is a major aging mechanism causing rapid degradation and fundamental safety risks [9–14]. The relevant factors for deposition of metallic Li on the surface of Si/graphite anodes are crucial to improve the performance and safety of state-of-the-art Li-ion batteries. Experimental works by Flügel et al. [15] as well as Yang et al. [16] highlight a decreasing risk of plating with increasing Si content in the composite anodes. The dominating effect is the reduction of the thickness of the anode coating which reduces the transport limitations at a constant areal capacity. On the other hand, Chen et al. [17] report in their simulation study an increasing risk of plating due to the typically low Li chemical diffusion coefficient of Si. A major challenge to gain a comprehensive understanding of the critical properties and parameters of plating in Si/graphite composites is the large number of different graphite and Si or $SiO_x$ materials used in different studies. Recently, Tao et al. [18] demonstrated that the Si source has a significant effect on plating in composite electrodes. In addition, the electrode microstructure and material morphology can affect plating in complex electrode structures [19].

By using simulation studies it is possible to disentangle the interplay between different materials in model geometries [20] as well as complex microstructures [21]. Simplified models or structures are helpful to break down the problem, as they allow parameter sensitivity analysis in general [22–25]. Within the last years, a significant number of models

---

[*] Corresponding author at: German Aerospace Center, Institute of Engineering Thermodynamics, Pfaffenwaldring 38-40, Stuttgart, 70569, Germany.
*E-mail address:* timo.danner@dlr.de (T. Danner).

https://doi.org/10.1016/j.electacta.2024.145010
Received 17 May 2024; Received in revised form 2 August 2024; Accepted 2 September 2024

of Si/graphite electrodes have been published in the literature [17,21,26–34]. Furthermore, recent work that addressed the aspect of plating in Si/graphite composite electrodes emphasized the importance of the topic [15–18,35–38]. Due to different materials or model assumptions, the published model and material parameters deviate by orders of magnitude. Significant differences in the prediction of plating can be expected when using these parameters in electrochemical simulations. However, a systematic analysis of the impact of varying parameters on plating is still missing.

Several models of plating on graphite and Si/graphite electrodes have been published in the literature [10,19,20,37,39–44]. While most of these articles use homogenized Newman-type models, only few attempts have been made to track plating directly in the complex electrode microstructure [10,19,39,41,42]. In the latter approach, the relevant transport phenomena within the complex structure are intrinsically captured and provide direct coupling between the particle morphology, electrode microstructure, and degradation processes, including the deposition of metallic Li. High resolution imaging e.g. using focused ion beam milling with scanning electron microscopy (FIB/SEM) is important to capture structural details of pores, passive and active materials [45].

In this work, we investigate the influence of different electrochemical parameters on plating in simple model geometries and complex electrode microstructures during galvanostatic charging. A 3D model system consisting of two equally sized spherical particles, which represent graphite and Si or $SiO_x$, is utilized to investigate the impact of varying electrochemical parameters on plating on the particle surface. Therefore, values for the chemical diffusion constant of Li in the active materials, the electronic conductivity, the open-circuit potential of active material versus Li, and the rate constant of the Faradaic reaction are compiled from literature and used in physico-chemical simulations. Subsequently, we use FIB/SEM tomography data of a commercial Si/graphite composite anode as input for half-cell simulations to investigate lithiation and metallic Li deposition for varying C-rates in a complex microstucture. The simulation study provides an improved understanding of the relevant parameters that affect Li plating and, ultimately, will enable optimization of the design of Si/graphite composite electrodes.

## 2. Methods

### 2.1. Model description

Simulations in this work are based on the model developed by Latz and Zausch [47] which was extended by Hein et al. [10,41] to include the effect of Li plating. Detailed derivations of the model equations can be found in the original publications. In this section, we briefly summarize the governing equations for an isothermal setup.

The transport of Li in the active material as a function of time $t$ is given by

$$0 = \frac{\partial c_s^{\mathrm{mat}}}{\partial t} + \boldsymbol{\nabla} \cdot \underbrace{\left(-D_s^{\mathrm{mat}} \boldsymbol{\nabla} c_s^{\mathrm{mat}}\right)}_{\boldsymbol{N}_s^{\mathrm{mat}}}. \tag{1}$$

$c_s^{\mathrm{mat}}$ is the concentration of Li in active material mat ∈ {Gr, Si} and $D_s^{\mathrm{mat}}$ the corresponding chemical diffusion coefficient. The charge conservation equation in the solid phase is used to calculate the electrostatic potential $\phi_s^{\mathrm{mat}}$. The electronic current $\boldsymbol{j}_s^{\mathrm{mat}}$ is determined by the local gradient in $\phi_s^{\mathrm{mat}}$ and the electronic conductivity $\kappa_s^{\mathrm{mat}}$ of the materials:

$$0 = \boldsymbol{\nabla} \cdot \underbrace{\left(-\kappa_s^{\mathrm{mat}} \boldsymbol{\nabla} \phi_s^{\mathrm{mat}}\right)}_{\boldsymbol{j}_s^{\mathrm{mat}}}. \tag{2}$$

Transport in the electrolyte is described by conservation equations of mass and charge according to

$$0 = \frac{\partial \varepsilon_e c_e}{\partial t} + \boldsymbol{\nabla} \cdot \underbrace{\left(-D_e^{\mathrm{eff}} \boldsymbol{\nabla} c_e + \frac{t_+ \boldsymbol{j}_e}{F}\right)}_{\boldsymbol{N}_e} \tag{3}$$

$$0 = \boldsymbol{\nabla} \cdot \underbrace{\left(-\kappa_e^{\mathrm{eff}} \boldsymbol{\nabla} \varphi_e + \frac{\kappa_e^{\mathrm{eff}}(1-t_+)RT}{F} \frac{\partial \mu_e}{\partial c_e} \boldsymbol{\nabla} c_e\right)}_{\boldsymbol{j}_e}. \tag{4}$$

The variable $\varepsilon_e$ is the porosity of materials with pore sizes below the resolution limit of our simulations. In the present study, this refers to the conductive additive and binder domain (CBD). The effective transport parameters $\Lambda^{\mathrm{eff}} \in \{\kappa^{\mathrm{eff}}, D^{\mathrm{eff}}, \ldots\}$ are calculated depending on bulk material properties $\Lambda$, porosity $\varepsilon$, and tortuosity $\tau$, namely $\Lambda^{\mathrm{eff}} = \varepsilon \cdot \tau^{-1} \cdot \Lambda$. More details can be found in the work of Knorr et al. [48]. Note that in the bulk electrolyte $\varepsilon_e$ equals one and the effective transport parameters correspond to bulk material parameters of the electrolyte. At the interface between electrolyte and anode active materials, we consider both intercalation and plating reactions following a general Butler-Volmer type expression. Thus, the intercalation current between electrolyte and active material is given by

$$i^{\mathrm{mat}} = i_0^{\mathrm{mat}} \left( exp\left(\frac{\alpha_a F}{RT} \eta^{\mathrm{mat}}\right) - exp\left(-\frac{(1-\alpha_a)F}{RT} \eta^{\mathrm{mat}}\right)\right) \tag{5}$$

$$i_0^{\mathrm{mat}} = i_{00}^{\mathrm{mat}} (c_e)^{\alpha_a} \left(c_s^{\mathrm{mat},max} - c_s^{\mathrm{mat}}\right)^{\alpha_a} (c_s^{\mathrm{mat}})^{1-\alpha_a} \tag{6}$$

$$\eta^{\mathrm{mat}} = \phi_s^{\mathrm{mat}} - \varphi_e - U_{0,\mathrm{mat}}(c_s^{\mathrm{mat}}). \tag{7}$$

Similarly, the plating/stripping current on the particle surface is described by

$$i_{Pl/St}^{\mathrm{mat}} = i_{Pl/St}^{00} \cdot c_e^{0.3} \cdot \left( exp\left(\frac{0.3F}{RT} \eta_{Pl/St}^{\mathrm{mat}}\right) - exp\left(-\frac{0.7F}{RT} \eta_{Pl/St}^{\mathrm{mat}}\right)\right) \tag{8}$$

$$\eta_{Pl/St}^{\mathrm{mat}} = \phi_s^{\mathrm{mat}} - \varphi_e + \frac{RT}{F} \cdot ln\left(\frac{n_{Pl,\mathrm{mat}}^4}{n_{Pl,0}^4 + n_{Pl,\mathrm{mat}}^4}\right). \tag{9}$$

Additionally, the model includes chemical intercalation of plated Li according to

$$N_{Ch.Int.}^{\mathrm{mat}} = N_{Ch.Int.}^{00} \cdot \left(c_s^{\mathrm{mat}}\right)^{0.5} \cdot \left( exp\left(\frac{0.5F}{RT} \eta_{Ch.Int.}^{\mathrm{mat}}\right) - exp\left(-\frac{0.5F}{RT} \eta_{Ch.Int.}^{\mathrm{mat}}\right)\right) \tag{10}$$

$$\eta_{Ch.Int.}^{\mathrm{mat}} = -U_{0,\mathrm{mat}}(c_s^{\mathrm{mat}}) - \frac{RT}{F} \cdot ln\left(\frac{n_{Pl,\mathrm{mat}}^4}{n_{Pl,0}^4 + n_{Pl,\mathrm{mat}}^4}\right). \tag{11}$$

We keep track of the amount of Li on the surface by solving

$$\frac{\partial n_{Pl,\mathrm{mat}}}{\partial t} = \left(N_{Ch.Int.}^{\mathrm{mat}} - \frac{i_{Pl/St}^{\mathrm{mat}}}{F}\right) \cdot A_{Pl,\mathrm{mat}}, \tag{12}$$

where $A_{Pl,\mathrm{mat}}$ is the particle surface area covered by plated Li. Note that the active surface area with CBD is scaled by the CBD porosity.

$$\boldsymbol{N}_s^{\mathrm{mat}} \cdot \boldsymbol{n} = \left(\frac{A_{Pl,\mathrm{mat}}}{A_{Total,\mathrm{mat}}} \cdot N_{Ch.Int.}^{\mathrm{mat}} + \left(1 - \frac{A_{Pl,\mathrm{mat}}}{A_{Total,\mathrm{mat}}}\right) \cdot \frac{i^{\mathrm{mat}}}{F}\right) \cdot \varepsilon_e \tag{13}$$

$$\boldsymbol{N}_e \cdot \boldsymbol{n} = \left(\frac{A_{Pl,\mathrm{mat}}}{A_{Total,\mathrm{mat}}} \cdot \frac{i_{Pl/St}^{\mathrm{mat}}}{F} + \left(1 - \frac{A_{Pl,\mathrm{mat}}}{A_{Total,\mathrm{mat}}}\right) \cdot \frac{i^{\mathrm{mat}}}{F}\right) \cdot \varepsilon_e \tag{14}$$

$$\boldsymbol{j}_s^{\mathrm{mat}} \cdot \boldsymbol{n} = \left(\frac{A_{Pl,\mathrm{mat}}}{A_{Total,\mathrm{mat}}} \cdot i_{Pl/St}^{\mathrm{mat}} + \left(1 - \frac{A_{Pl,\mathrm{mat}}}{A_{Total,\mathrm{mat}}}\right) \cdot i^{\mathrm{mat}}\right) \cdot \varepsilon_e + j_s^{CBD} \tag{15}$$

$$\boldsymbol{j}_e \cdot \boldsymbol{n} = \left(\frac{A_{Pl,\mathrm{mat}}}{A_{Total,\mathrm{mat}}} \cdot i_{Pl/St}^{\mathrm{mat}} + \left(1 - \frac{A_{Pl,\mathrm{mat}}}{A_{Total,\mathrm{mat}}}\right) \cdot i^{\mathrm{mat}}\right) \cdot \varepsilon_e. \tag{16}$$

In this study, we additionally consider exchange of Li between graphite ($\mathrm{mat}_1$) and Si ($\mathrm{mat}_2$) or vice versa. Driving force of the process is the chemical potential represented by the open-circuit potential $U_{0,\mathrm{mat}_j}$,

**Table 1**
List of symbols.

| Symbol | Unit | Value[a] | Description |
|---|---|---|---|
| $c_s$ | mol/cm$^3$ | | Li concentration in solid phase |
| $c_s^{max}$ | mol/cm$^3$ | | Maximum solid phase Li concentration |
| $c_s^0$ | mol/cm$^3$ | | Initial solid phase Li concentration |
| $x_s$ | – | | Lithiation fraction |
| $D_s$ | cm$^2$/s | | Diffusion coefficient of solid phase |
| $\boldsymbol{N}_s$ | mol/(cm$^2$ s) | | Ion flux in solid phase |
| $\kappa_s$ | S/cm | | Electronic conductivity of solid phase |
| $\phi_s$ | V | | Electric potential of solid phase |
| $\boldsymbol{j}_s$ | A/cm$^2$ | | Current density in solid phase |
| $c_e$ | mol/cm$^3$ | | Concentration in electrolyte phase |
| $c_e^0$ | mol/cm$^3$ | $10^{-3}$ | Initial concentration in electrolyte phase |
| $D_e$ | cm$^2$/s | See SI of [46] | Diffusion coefficient of electrolyte phase |
| $t_+$ | – | See SI of [46] | Transference number |
| $\boldsymbol{j}_e$ | A/cm$^2$ | | Current density in electrolyte phase |
| $\boldsymbol{N}_e$ | mol/(cm$^2$ s) | | Ion flux in electrolyte phase |
| $\kappa_e$ | S/cm | See SI of [46] | Ionic conductivity of electrolyte phase |
| $\varepsilon_e$ | – | 0.5 | Porosity within CBD and separator, else set to 1 |
| $\tau_{\mathrm{CBD},e}^{-1}$ | – | 0.2 | Inverse effective tortuosity in liquid CBD phase |
| $\varphi_e$ | V | | Electrochemical potential of electrolyte phase |
| $T$ | K | 298.15 | Temperature |
| $\mu_e$ | J/mol | | Chemical potential |
| $i$ | A/cm$^2$ | | Current density |
| $i_{00}$ | Acm$^{2.5}$/mol$^{1.5}$ | | Exchange current density |
| $\alpha_a$ | – | 0.5 | Anodic transfer coefficient |
| $\eta$ | V | | Overpotential |
| $U_0$ | V | | Equilibrium potential |
| $N^{\mathrm{mat}_1,\mathrm{mat}_2}$ | mol/(cm$^2$ s) | | Li flux between adjacent active materials |
| $N_{00}^{\mathrm{mat}_1,\mathrm{mat}_2}$ | cm/s | $3.2775 \cdot 10^{-7}$ | Reaction rate for adjacent active materials |
| $\eta_{Pl/St}$ | V | | Overpotential of plating reaction |
| $n_{Pl}$ | – | | Number of mono layers of plated Li |
| $n_{Pl,0}$ | – | $10^{-10}$ | Initial number of mono layers of plated Li |
| $i_{Pl/St}$ | A/cm$^2$ | | Current density for plated Li |
| $i_{Pl/St}^{00}$ | A/(cm$^{1.1}$ mol$^{0.3}$) | 0.0631 | Exchange current density for plated Li |
| $\eta_{Ch.Int.}$ | V | | Overpotential of chemical intercalation |
| $N_{Ch.Int.}$ | mol/(cm$^2$ s) | | Li flux between solid phase and plated Li |
| $N_{Ch.Int.}^{00}$ | mol$^{0.5}$/(cm$^{0.5}$ s) | $1.0364 \cdot 10^{-9}$ | Chemical intercalation rate constant |
| $A_{Pl}$ | cm$^2$ | | Surface area covered by plated Li |
| $A_{Total}$ | cm$^2$ | | Active material surface area |
| $\kappa_{CBD}$ | S/cm | 10 | Electronic conductivity of conductive CBD phase |
| $\tau_{\mathrm{CBD},s}^{-1}$ | – | 2 | Inverse effective tortuosity in conductive CBD phase |
| $\tau_{\mathrm{sep}}^{-1}$ | – | 0.7071 | Inverse effective tortuosity within separator |

[a] Stated if the same is applied for all simulations.

$j \in \{1, 2\}$. The transfer of Li between two active materials is described by

$$N^{\mathrm{mat}_1,\mathrm{mat}_2} = N_{00}^{\mathrm{mat}_1,\mathrm{mat}_2} \cdot (c_s^{\mathrm{mat}_1} c_s^{\mathrm{mat}_2})^{0.5} \cdot 2sinh\left(\frac{F}{RT}\left(U_{0,\mathrm{mat}_1}(c_s^{\mathrm{mat}_1}) - U_{0,\mathrm{mat}_2}(c_s^{\mathrm{mat}_2})\right)\right), \quad (17)$$

$$\boldsymbol{N}_s^{\mathrm{mat}_1} \cdot \boldsymbol{n} = -\boldsymbol{N}_s^{\mathrm{mat}_2} \cdot \boldsymbol{n}. \quad (18)$$

Symbols used throughout this work are summarized in Table 1.

### 2.2. Model parameters

At the beginning of a simulation using physico-chemical models, several parameters must be specified. While geometric parameters such as electrode thickness, width, and length are typically known or experimentally accessible, others such as electrode composition or particle size can be determined from tomography data. Finally, physico-chemical parameters require model experiments or a fit to electrochemical data. For this class of parameters, the measurement uncertainties and deviations from the values reported in the literature are the largest. A summary of experimental techniques for parameterization can be found in [45].

In our study, we focus on four physico-chemical parameters that influence transport and kinetics into and within the active material of the Si/graphite composite electrode. Parameters of the electrolyte and other materials are summarized in Table 1. Relevant parameters in our study are the chemical diffusion coefficient of Li in the active material, the electronic conductivity of the active material, the open-circuit potential of the active material, and the rate constant of the Butler-Volmer expression for the intercalation current. Note that the parameters of one material also affect the lithiation and plating of the other material, and the interactions can be complex. This is a common effect reported for Si/graphite composites [17,18,20,26,29,49–51].

In this work, we present a parameter study covering the range of values reported in the modeling literature and existing databases (e.g. LiionDB [52]) for Li-ion battery models. Although providing a comprehensive overview of Si and graphite model parameters published in literature, we do not aim to give a complete review of the existing literature. Note that model parameters for graphite are typically in a similar range and there is some consistency between different studies, while the differences for Si materials are much larger. This is due to different morphologies and chemical compositions of Si materials published in the literature. Moreover, crystalline Si is known to become gradually amorphous during cycling which also has a significant impact on material properties. In our study, we assume that parameters are representative of materials after several formation cycles. Therefore, the focus of this study is primarily on the effect of variations in the properties of the Si active materials.

#### 2.2.1. Open-circuit potential

The main thermodynamic parameter of an active material is the open-circuit potential (OCP), commonly measured or expressed against

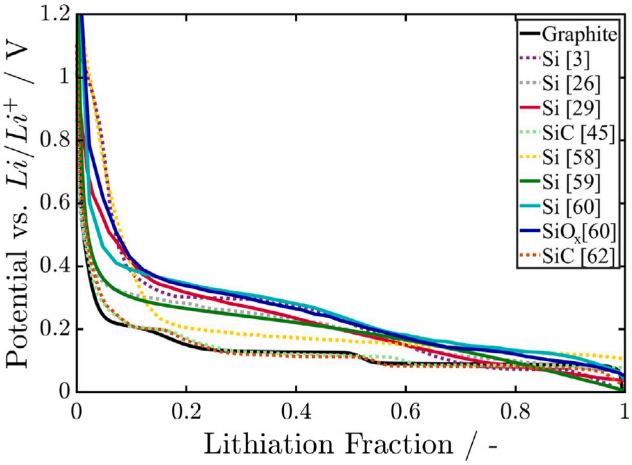

**Fig. 1.** Overview of relevant lithiation OCP curves found in literature. Solid lines indicate OCPs considered in parameter study.

a Li metal electrode. The OCP changes as function of the Li concentration $c_s^{\mathrm{mat}}$ of the respective material. Often the galvanostatic intermittent titration technique (GITT) is used to retrieve the equilibrium potential [29] as function of relative Li content. Typically, fits of the OCP are provided as function of normalized Li concentration $x_s^{\mathrm{mat}}$, expressed as

$$x_s^{\mathrm{mat}} = \frac{c_s^{\mathrm{mat}}}{c_s^{\mathrm{mat},max}}, \tag{19}$$

where $c_s^{\mathrm{mat},max}$ is the maximum Li concentration or specific capacity of the respective material.

For graphite we use in our study the OCP obtained within the work of Hogrefe et al. [53] (details provided in the Supplementary Material). Si shows a significant hysteresis between lithiation and delithiation [32,54–57] which is mainly attributed to the dependence of electric potential on the stress in lithiated Si [4]. We focus on reported lithiation curves as they are relevant for charging and Li plating. Although mechanics are out of the scope of this paper, the stress caused by Li alloying induced swelling of Si particles is therefore implicitly included in the simulations. Additional stress caused by e.g. the housing of the electrodes was found to be in the order of 5 MPa for cylindrical cells with moderate Si content. The estimated effect on the OCV assuming stress potential coupling of 62 mV/GPa is less than 1 mV and neglected in our simulations. Fig. 1 gives an overview of Si lithiation OCPs found in literature. OCP curves of the different Si materials differ due to morphology, chemistry, and carbon content. Chandrasekaran et al. ([3], purple dotted line), Ding et al. ([58], yellow dotted line), and Kolzenberg et al. ([59], dark green solid line) consider nanometer sized particles. In contrast, micro-Si is applied by Pereira et al. ([26], gray dotted line) and Lory et al. ([29], red solid line). Pan et al. ([60], cyan and blue solid lines) study both Si and SiO$_x$. Their detailed experimental analysis was already utilized in [61] for simulations. Finally, Sturm et al. ([62], brown dotted line) and Chen et al. ([45], bright green dotted line) consider composite materials with high graphite fractions resulting in similar OCPs compared to the graphite reference OCP ([53], black solid line). An analytic expression for the Si OCP function is provided by Kolzenberg et al. [59]

$$U_{0,\mathrm{Si}}(x_s^{\mathrm{Si}}) = \frac{-0.2453\left(x_s^{\mathrm{Si}}\right)^3 - 0.00527\left(x_s^{\mathrm{Si}}\right)^2 + 0.2477 x_s^{\mathrm{Si}} + 0.006457}{x_s^{\mathrm{Si}} + 0.002493}. \tag{20}$$

In other cases, we extract OCPs from the image data and interpolate between tabulated values provided in Table S1. As the number of different OCPs is restricted in the following study, those included in the study are indicated by solid lines in Fig. 1.

**Table 2**
Summary of the chemical diffusion coefficients $D_s^{\mathrm{mat}}$ [cm$^2$/s] found in literature.

| $D_s^{\mathrm{Gr}}$ | References | $D_s^{\mathrm{Si}}$ | References | $D_s^{\mathrm{SiC}}$ | References |
|---|---|---|---|---|---|
| $10^{-11} - 10^{-7}$ | [63–65] | $3 \cdot 10^{-10}$ | [66] | $5 \cdot 10^{-10}$ | [62] |
| $9 \cdot 10^{-10}$ | [67,68] | $1.67 \cdot 10^{-10}$ | [27,32,69] | $2.4 \cdot 10^{-10}$ | [70] |
| $7 \cdot 10^{-10}$ | [66] | $2 \cdot 10^{-11}$ | [71,72] | $1.74 \cdot 10^{-11}$ | [45] |
| $5.5 \cdot 10^{-10}$ | [27,32,73] | $3 \cdot 10^{-12}$ | [33,72] | | |
| $3.9 \cdot 10^{-10}$ | [10,33,74,75] | $2 \cdot 10^{-12}$ | [76] | | |
| | [77–79] | $10^{-12}$ | [26,58,80] | | |
| $3.4558 \cdot 10^{-10}$ | [46] | | [81] | | |
| $2 \cdot 10^{-10}$ | [26,40,82,83] | $10^{-13}$ | [59,84,85] | | |
| $10^{-10}$ | [86] | $(2 - 3.5) \cdot 10^{-14}$ | [87] | | |
| $10^{-11}$ | [88] | $10^{-14}$ | [3] | | |

### 2.2.2. *Chemical diffusion coefficient*

We model the diffusion of Li within active particles by Fick's law as given in Eq. (1). Values of the chemical diffusion coefficient $D_s^{\mathrm{mat}}$ reported in the literature are listed in Table 2. Note that values for both graphite and Si materials vary by several orders of magnitude. Generally, particle size and shape affect calculations of apparent diffusion coefficients. Additionally, the SEI or cracks and micropores in the materials affect the Li transport in the particles and extracted effective chemical diffusion coefficients accordingly. The range reported for graphite is between $10^{-9}$ and $10^{-11}$ cm$^2$/s. However, majority of considered studies report chemical diffusion coefficients between $2-4 \cdot 10^{-10}$ cm$^2$/s. In our simulation study, we use a chemical diffusion coefficient of $2 \cdot 10^{-10}$ cm$^2$/s as standard parameter for graphite.

For Si materials the large volume expansion and corresponding changes in molar volume, electrode tortuosity, surface area, and morphology add to errors in measured chemical diffusion coefficients. In their comprehensive characterization of Si and SiO$_x$ material, Pan et al. [60] report that the diffusion coefficient in SiO$_x$ particles is one order of magnitude larger compared to micrometer sized Si particles. Moreover, diffusion coefficients in these micro-Si particles are one order of magnitude larger than those in nano-Si particles.

Since some models or measurement techniques do not differentiate between the Si and graphite in the composite, in Table 2 and the following two tables a column for SiC is added.

### 2.2.3. *Exchange current density*

The next electrochemical parameter dealt with in the parameter study is the exchange current density of the Li intercalation reaction, $i_0^{\mathrm{mat}}$. The exchange current density is correlated with the active surface area of the materials. Therefore, we expect, and indeed observe, significant variability in the reported values [89]. In general, the exchange current density can be calculated from the charge transfer resistance measured by electrochemical impedance spectroscopy (EIS) or determined by fit to rate experiments. The Faradaic current density, the current associated with the electrochemical reaction at the solid-electrolyte interface, is in our model described by the Butler Volmer Equation (5).

In Table 3, we provide values for the exchange current density factor $i_{00}^{\mathrm{mat}}$. In our simulation study, the impact of varying $i_{00}^{\mathrm{mat}}$ is analyzed and $i_{00}^{\mathrm{Gr}} = 0.079$ Acm$^{2.5}$/mol$^{1.5}$ is taken as standard. Exchange current density factors reported for graphite vary within a comparatively small range. However, as also pointed out by Verma et al. [84], there is a significant spread in the values reported for Si.

### 2.2.4. *Electronic conductivity*

Lastly, electronic current in the active material (see Eq. (2)) is governed by the electric conductivity of the materials $\kappa_s^{\mathrm{mat}}$. Typical values reported in the literature for graphite, $\kappa_s^{\mathrm{Gr}}$, and Si, $\kappa_s^{\mathrm{Si}}$, are listed in Table 4. Note that effective conductivities are commonly measured on the electrodes or compressed powders which are expected to be generally lower compared to the electronic conductivity of the bulk

**Table 3**
Summary of the exchange current density factors $i_{00}^{\text{mat}}$ [Acm$^{2.5}$/mol$^{1.5}$] found in literature.

| $i_{00}^{\text{Gr}}$ | References | $i_{00}^{\text{Si}}$ | References | $i_{00}^{\text{SiC}}$ | References |
|---|---|---|---|---|---|
| 23.638825[a] | [26] | 24.1212[a] | [3] | 0.2895[a] | [62] |
| 1.497019[b] | [90] | 19.297[a] | [26] | | |
| 0.367[a] | [79] | 0.57891[a] | [33] | | |
| 0.1879299[b] | [74] | 0.0648[a,a] | [32,45] | | |
| 0.1447[a] | [88] | 0.0096485[a] | [66] | | |
| 0.1397[a] | [91] | $9.6485 \cdot 10^{-4}$[a] | [80] | | |
| 0.1098933[b] | [92] | $1.73673 \cdot 10^{-5}$[a] | [84] | | |
| 0.096485[a] | [66] | | | | |
| 0.088 | [10] | | | | |
| 0.0790[a] | [83] | | | | |
| 0.0648[a,a] | [32,45] | | | | |
| 0.0254 | [46] | | | | |
| 0.002 | [86] | | | | |

[a] Multiplied by Faraday constant to fit model definition.

[b] Determined by given $i_0^{\text{mat}}$ and concentration.

**Table 4**
Summary of the electronic conductivities $\kappa_s^{\text{mat}}$ [S/cm] found in literature.

| $\kappa_s^{\text{Gr}}$ | References | $\kappa_s^{\text{Si}}$ | References | $\kappa_s^{\text{SiC}}$ | References |
|---|---|---|---|---|---|
| 21.2 | [93] | 1 | [81] | 10 | [66,70] |
| 10 | [10,86,94] | 0.33 | [33,80,95] | 2.15 | [32,45] |
| 1 | [40,46,67,68] | 0.01 | [27] | 1 | [62] |
| | [73,74,79] | $6.7 \cdot 10^{-4}$ | [96] | | |
| $0.139 \pm 0.034$ | [91] | | | | |

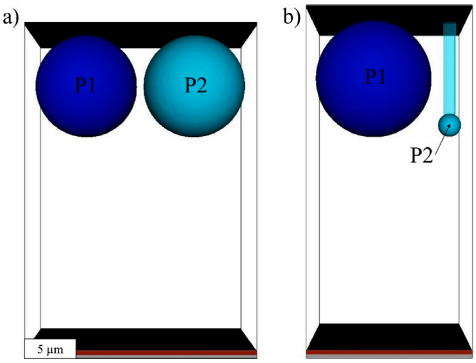

$c_s^{\text{P1},max}$ [29]
$30032 \cdot 10^{-6}$ mol/cm$^3$
$c_s^{\text{P2},max}$ [29]
$272030 \cdot 10^{-6}$ mol/cm$^3$
$x_s^{\text{mat},0}$ 0.01
OCP Eq. (S1) [53]
$D_s^{\text{mat}}$ [83]
$2 \cdot 10^{-10}$ cm$^2$/s
$i_{00}^{\text{mat}}$ [83]
0.0079 Acm$^{2.5}$/mol$^{1.5}$
$\kappa_s^{\text{mat}}$ 1 S/cm [74]

**Fig. 2.** Visualization of geometry of model half-cell with two (a) equally and (b) unequally sized particles representing graphite (P1, dark blue) and Si (P2, cyan) next to an overview of the standard input values.

materials. The first column provides effective electronic conductivities of graphite electrodes including binder and conductive additives. The second column provides data on Si containing electrodes, while the third column gives an overview of composite electrodes. In our study, we use an electric conductivity of graphite of 1 S/cm as standard.

## 2.3. Simulation methodology

In this study, we use two different setups to investigate plating in Si/graphite composite electrodes. We perform an extensive simulation study in a *simplified half-cell* model geometry consisting of two spherical particles. In a second step, we investigate plating in a *complex electrode microstructure* of a Si/graphite anode retrieved from a commercial cell.

### 2.3.1. Model half-cell geometry

*Simulation domain.* Fig. 2(a) shows the setup employed in the parameter study consisting of two geometrically identical spherical particles with a diameter of 10 µm, later on referred to as particle 1 (P1, dark blue) and particle 2 (P2, cyan). The two particles are attached to a current collector (CC, dark gray) and are 0.5 µm apart from each other. The particles are surrounded by liquid electrolyte. Between the particles and the Li metal counter electrode shown in brown color is a 20 µm thick porous separator. The separator is soaked with liquid electrolyte (50 % porosity resulting in $\tau_{\text{sep}}^{-1} = 0.7071$). The resolution of the simulation domain is 0.1 µm and we apply periodic boundary conditions.

Fig. 2(b) shows a slightly modified setup wherein the diameter of the first particle is increased to 11.7 µm and the diameter of the second particle is reduced to 2.4 µm. This reflects the average particle sizes of graphite and Si in the tomography data of the commercial cell described in Section 2.3.2 [45]. The transparent cyan area indicates electronic connection to the current collector (material with 90 % porosity and high electric conductivity of 1000 S/cm). Note that the setup was chosen to minimize impact on electrolyte transport and to ensure that the surface of particles 1 and 2 have the same distance to the Li metal counter electrode.

*Simulation procedure.* In order to investigate the effect of electrode composition on lithiation and plating, the aim of the simplified model geometries is to reduce complexity and focus on the effect of physicochemical parameters only. In a first step, we set parameters of particle 1 and 2 equal to the standard values of graphite provided in Fig. 2 and discussed above. Exception is the specific capacity of the materials represented by the maximum concentration. $c_s^{\text{P2},max}$ corresponds to the theoretical capacity of Si. In the subsequent study, we keep three of the four material parameters constant and vary only the fourth material parameter. Lithiation and plating behavior is studied by simulating constant current lithiation and plating with 1 C rate for up to 1 h.

### 2.3.2. Complex electrode microstructure

*Simulation domain.* Transfer to state-of-the-art electrode geometries is crucial to account for realistic particle shapes in complex and realistic electrode microstructures with state-of-the-art composition. In order to analyze Li plating in realistic Si/graphite electrode geometries, we image and analyze the anode of a commercial LG INR21700-M50T cell. This or similar cells have been also investigated in [32,45,97].

A 3D reconstruction of the microstructure of the Si/graphite composite anode is obtained via FIB/SEM tomography. The methodology is described in detail in the Supplementary Material. The reconstruction representing a fraction of the electrode volume has a size of $30 \times 35 \times 46$ µm$^3$ with the z-direction pointing in the direction from CC to separator. The voxel size of the reconstruction is $80 \times 80 \times 80$ nm$^3$. For the simulations, the voxel size is increased to $160 \times 160 \times 160$ nm$^3$ in order to decrease the computational cost. Note that the image operation did not change the composition of the electrode. For the generation of a digital twin of the composite anode, the structure is mirrored in $z$-direction and cropped to an electrode thickness of 85.2 µm [32]. Finally, we add CBD with 50 % porosity [98]. The volume fractions of the electrode are 15.9 vol% electrolyte, 79.7 vol% graphite, 1.8 vol% Si, and 2.5 vol% CBD. The composition obtained from FIB/SEM tomography is in good agreement with previous studies on these electrodes. Due to the low Si content, we neglect volume changes in our simulations [34].

Finally, we assemble virtual cells comprising an anode CC, a Li metal counter electrode, a 20 µm thick separator, the Si/graphite composite electrode, and a cathode CC. The resulting digital twin of a half-cell with the anode of the LG INR21700-M50T cell is depicted in Fig. 3.

*Simulation procedure.* Aim of the simulation study is to examine plating in a realistic 3D Si/graphite microstructure. To analyze the lithiation and plating behavior, we simulate lithiation with various currents up to 1 C. Material parameters for these simulations are summarized in Table 5 and specified based on how frequently they were used in other publications and how comparable those setups were to an LG INR21700-M50T anode. For example, SiO$_x$ [60] is a good OCP choice as it is deduced from GITT measurements on the mentioned

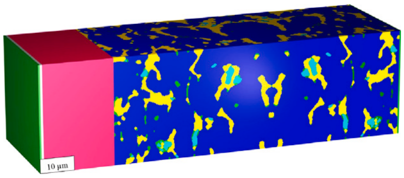

**Fig. 3.** Digital twin of a half-cell used to simulate Li plating. The microstructure of the Si/graphite composite electrode is obtained by FIB/SEM tomography of the anode material of an LG INR21700-M50T cell (left to right: CC in green, counter electrode in white, separator in red, electrolyte in yellow, CBD in green, graphite in dark blue, Si in cyan, CC in green).

**Table 5**
Summary of input parameters for simulations of the adjusted model setup and complex electrode microstructure.

| Parameters | | Graphite | Si |
|---|---|---|---|
| $c_s^{\mathrm{mat},0}$ | [mol/cm$^3$] | $300.32 \cdot 10^{-6}$ | $17\,321.95 \cdot 10^{-6}$ |
| OCP | [V] | Eq. (S1) | SiO$_x$ [60] |
| $D_s^{\mathrm{mat}}$ | [cm$^2$/s] | $3.9 \cdot 10^{-10}$ | $3 \cdot 10^{-12}$ |
| $\kappa_s^{\mathrm{mat}}$ | [S/cm] | 1 | 0.33 |
| $i_{00}^{\mathrm{mat}}$ | [Acm$^{2.5}$/mol$^{1.5}$] | 0.079 | 0.0096485 |

cell. Furthermore, the chosen chemical diffusion coefficient for Si is one of the higher values considered for $D_s^{\mathrm{P2/Si}}$ if those of carbon-mixed materials are neglected. This aligns with the fact that in the commercial anode SiO$_x$ is to some extent applied since this shows higher diffusion than Si [60]. The value is utilized in the rather recent publication of Jiang et al. [33] where micro meter sized particles are considered with a similar size proportion for Si and graphite as in the LG cell. Thus, it comes naturally to mind to choose Jiang et al.'s graphite diffusion coefficient as well. This choice is affirmed by the number of references that used $D_s^{\mathrm{Gr}} = 3.9 \cdot 10^{-10}$ cm$^2$/s already. $i_{00}^{\mathrm{Si}} = 0.0648$ Acm$^{2.5}$/mol$^{1.5}$ is from a recent publication of Chen et al. [66] that considers Si particles with a diameter of 2 μm in a Si/graphite anode as well.

## 3. Results and discussion

### 3.1. Model half-cell geometry

#### 3.1.1. Open-circuit potential

In a first step of investigating the effect of electrode composition on lithiation and plating, we apply the OCP of graphite to the first particle and use five different OCPs representing graphite and four Si materials for the second particle. The results of the 1 C lithiation simulations are shown in Fig. 4. Fig. 4(a) presents the half-cell voltage during lithiation. The graphite reference case shows generally the lowest cell voltage. At around 0.5 h the voltage drops below 0 V indicating the phase where the risk for Li plating increases. However, the cell voltage continues to decrease up to 0.92 h before we observe a constant cell voltage of around −50 mV. The constant cell voltage indicates full coverage of the particle surfaces with plated Li.

The change of P2 to the OCP of Si materials causes an increase of the cell voltage as it is commonly reported for Si/graphite composite electrodes. It is generally anticipated that, therefore, addition of Si reduces the risk of Li plating. Indeed we observe that simulations with a particle using Si OCP stay longer above 0 V during lithiation. However, they tend to decrease more rapidly afterwards, reaching constant voltage of −50 mV earlier compared to the graphite reference. Note that, although differences in the OCP are minor (cf. Fig. 1), there can be pronounced differences in the simulated cell voltage e.g. comparing Si and SiO$_x$ from [60].

Corresponding plating thicknesses are shown in Fig. 4(b). The simulation using the OCP representing the Si material of Lory et al. [29] shows a linear increase in plating thickness right after 0.8 h. As indicated by the constant cell voltage, other OCPs result in delayed onsets of plating and lower average thickness accordingly. Since lithiation of the particles is crucial to the onset of plating, we present maximal (abbreviated max) lithiation fractions in Fig. 4(c). Different symbols represent lithiation of P1 (asterisks, graphite) and P2 (open squares, variable OCP), respectively. For the graphite reference case (black) the lithiation fraction in both particles increases linearly over time. The onset of plating causes a noticeable change in the slope of the lithiation curves. Moreover, slight differences can be observed in the lithiation fraction of the two particles, which is due to the higher capacity of P2. In the other cases when P2 is representing different Si materials, P2 is lithiated preferentially due to the higher OCPs. The onset of plating is also clearly visible by a kink in the lithiation fraction of P1. Note that lithiation fractions increase despite coverage of the particle surfaces with plated Li which can be linked to the chemical intercalation of Li (Eq. (13)).

The corresponding 3D distributions of normalized Li concentration and plated Li thickness can be found in Fig. 4(d). On the left-hand side, we present the graphite reference case after 0.78, 0.86, 0.98, and 1 h of lithiation. Note that in all cases the cell voltage is well below 0 V. Lithiation of the particles is rather homogeneous with slightly higher concentrations close to the separator. As a result we also observe a higher plating thickness at the bottom of the particles. After 1 h, plating thickness ranges from 26 to 170 nm. Moreover, plating is more pronounced on P1. The only difference between P1 and P2 is the specific capacity of the particles. This indicates that the specific capacity of the materials is a factor influencing the distribution of plating on different materials. Considering identical particles with the same specific capacity yields not only identical results for both particles but also less plating than in all five cases considered here.

This trend is more pronounced when using the OCP of Si material [29] for P2. At all of the portrayed points in time, the lithiation fraction of P1 is lower than the one of P2. Nonetheless, we observe higher plating thickness on P1 and an overall higher amount of plated Li on both particles compared to the graphite reference case.

In conclusion, the higher OCP of Si increases the cell voltage. Therefore, cell voltage drops below 0 V at higher SOC. Still, Li plating starts earlier in the simulations with Si OCP and we predict preferential plating on the particle with graphite OCP and specific capacity.

#### 3.1.2. Chemical diffusion coefficient

The mobility of Li in the material is considered a key parameter for Li plating. Therefore, we simulate nearly 200 different setups employing the values listed in Table 2 plus additional intermediate points. Fig. 5 gives an overview of the simulation study. Results of the 1 C lithiation simulations are presented after 1000 s due to the sensitivity towards this parameter. The left column of the graph shows the maximal lithiation fraction (top) and plating thickness (bottom) on P1 representing graphite parameters. The right column of the graph shows the maximal lithiation fraction (top) and plating thickness (bottom) on P2 representing Si parameters. The range of parameters for graphite and Si are given by the x- and $y$-axis of the heat maps, respectively. Pink dots represent parameters reported in the literature and summarized in Table 2. Green squares indicate additional simulation parameters to support the evaluation within the parameter space. The asterisk highlights values which are used for further analysis in Sections 3.1.5 and 3.2. Generally, small diffusion coefficients increase the concentration gradient (see Supplementary Material) in the particles resulting in high surface concentration and low particle utilization. Therefore, low Li mobility is expected to increase the plating on the particle surface which is indeed observed in Fig. 5(c) and (d). In general, values reported for the chemical diffusion coefficient of Si are smaller than values reported for graphite materials. Therefore, we observe more plating on the surface of P2, representing Si material. Another interesting effect is the interaction of particles and the mutual influence of parameters on plating thickness on the other particle. The dashed horizontal line in Fig. 5(c) and (d) emphasizes simulations with the same P1 chemical diffusion

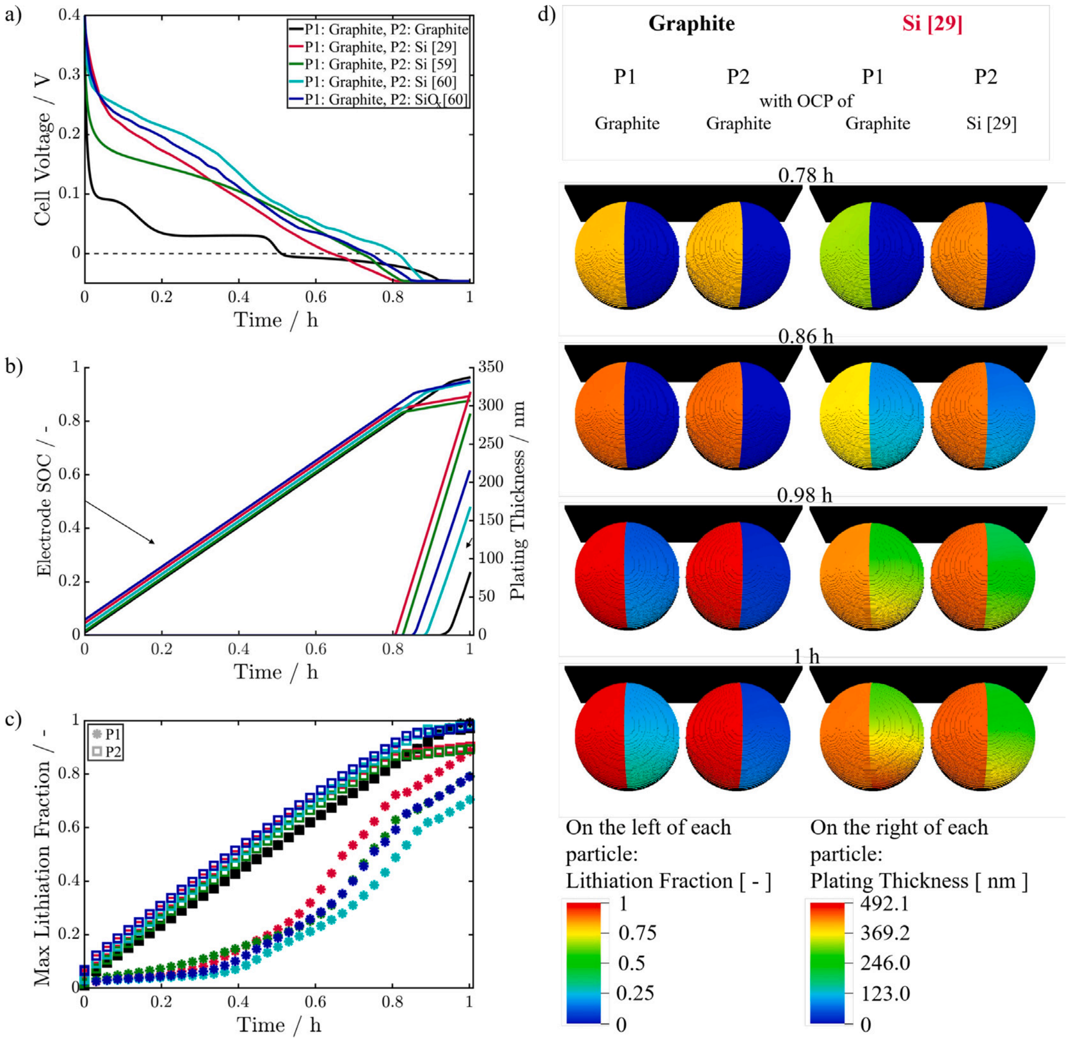

**Fig. 4.** Simulation results of 1 C lithiation in model half-cell geometry. The line colors indicate the OCP of P2 according to the legend in (a) while the OCP of P1 is in all cases representing graphite: (a) cell voltage, (b) SOC and average plating thickness in the whole electrode, (c) maximal lithiation fractions per material, and (d) 3D distributions of lithiation fraction and plating thickness comparing graphite and Si [29]/graphite composite.

coefficient, namely $D_s^{\mathrm{P1/Gr}} = 3.9 \cdot 10^{-10}$ cm$^2$/s. Following that line from right to left, one notices that decreasing the mobility of Li in P2 favors plating on the surface of P1. This is due to redistribution of current. Similar effects also produce a higher maximum Li concentration in Fig. 5(a). This demonstrates the complexity of the electrochemical processes that result in plating on the surface of the particles.

In general, the size of Si particles or the design of SiC composite materials need to be tuned to provide Li mobility similar to that in graphite to avoid negative impact of plating on the surface of both materials in the composite electrode.

In conclusion, lower Li mobility of Si as reported in the literature will result in a higher probability and amount of Li plating. The majority of the plating will be on the material with low Li mobility, however, also strongly affect plating on the material with higher Li mobility.

### 3.1.3. Exchange current density

Fig. 6 summarizes the results of 112 simulations with various exchange current density factors. Graphs (a) and (c) show the maximal lithiation fraction and plating thickness of P1 after 1000 s at a current density corresponding to 1 C rate. Corresponding data on P2 is presented in Fig. 6(b) and (d). Fig. 6(a) and (b) confirm that lithiation preferentially occurs in those particles that are kinetically favored. Therefore, the maximal lithiation fraction of P2 (Fig. 6(b)) is higher on the right hand side of the graph. The pattern is more complex in the case of P1. Due to faster kinetics we observe higher lithiation of P1 in the upper left-hand corner of Fig. 6(a). However, lithiation decreases in the lower left-hand corner. This is because of significant plating that is observed on P1 in this parameter range as shown in Fig. 6(c). The reason is that plated Li prevents further direct intercalation and utilization of the material. In this region, the cell voltage instantaneously drops below 0 V and we observe plating almost from the beginning. Additional data is provided in the Supplementary Material. In contrast, plating on P2 (Fig. 6(d)) is only observed in a narrow parameter window. Namely, if intercalation kinetics are slightly slower in P2 than in P1. However, if kinetics are too slow it will cause extensive plating on P1. The combination of slow kinetics and the nucleation barrier introduced by the plating model prevent plating on P2 in this regime. Again, this highlights complex interactions of materials determining the distribution of plating in composite electrodes. Note that the scales of the color legends in Fig. 6(c) and (d) differ by an order of magnitude. Generally, the plating thickness on P1 is much higher compared to P2.

In conclusion, we observe in our simulation significant impact of the intercalation rate on the distribution of plating and plating thickness.

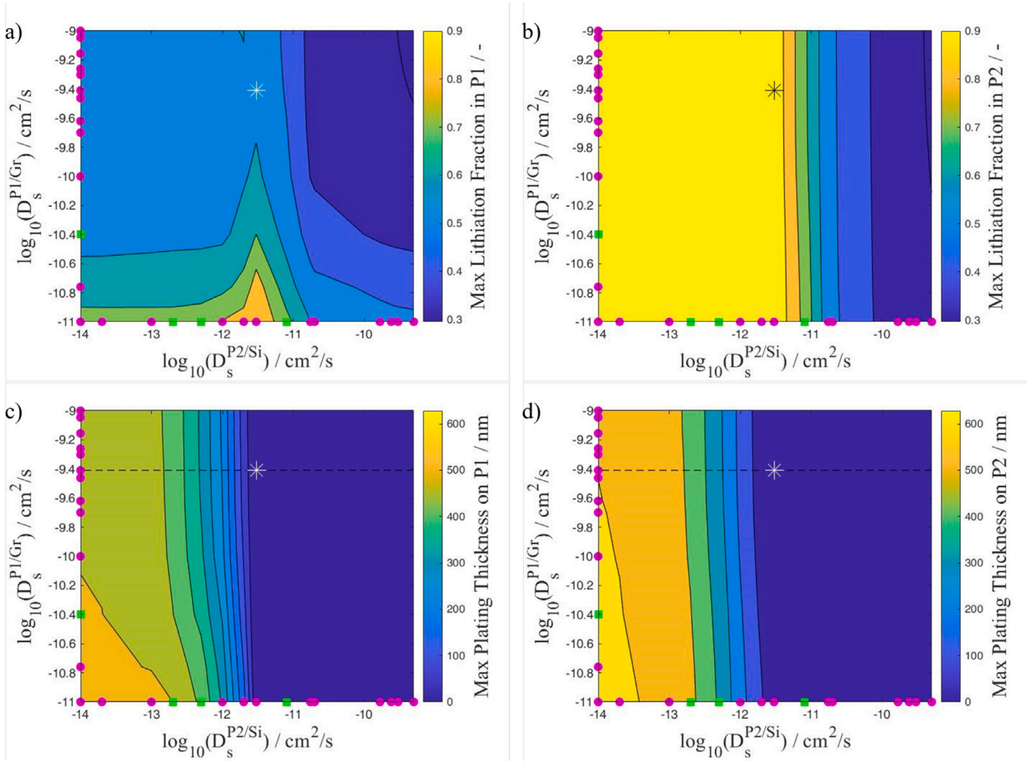

**Fig. 5.** Simulation results of 1 C lithiation of model half-cell geometry for varying $D_s^{\mathrm{mat}}$. Pink dots represent reported values in Table 2 and green squares represent additional auxiliary data points in the parameter space. Lithiation fraction (a) and plating thickness (c) on P1 (representing graphite) after 1000 s of lithiation are shown in the left column. Lithiation fraction (b) and plating thickness (d) on P2 (representing Si) are shown in the right column. The asterisk marks the combination of parameters used in simulations with the complex microstructure.

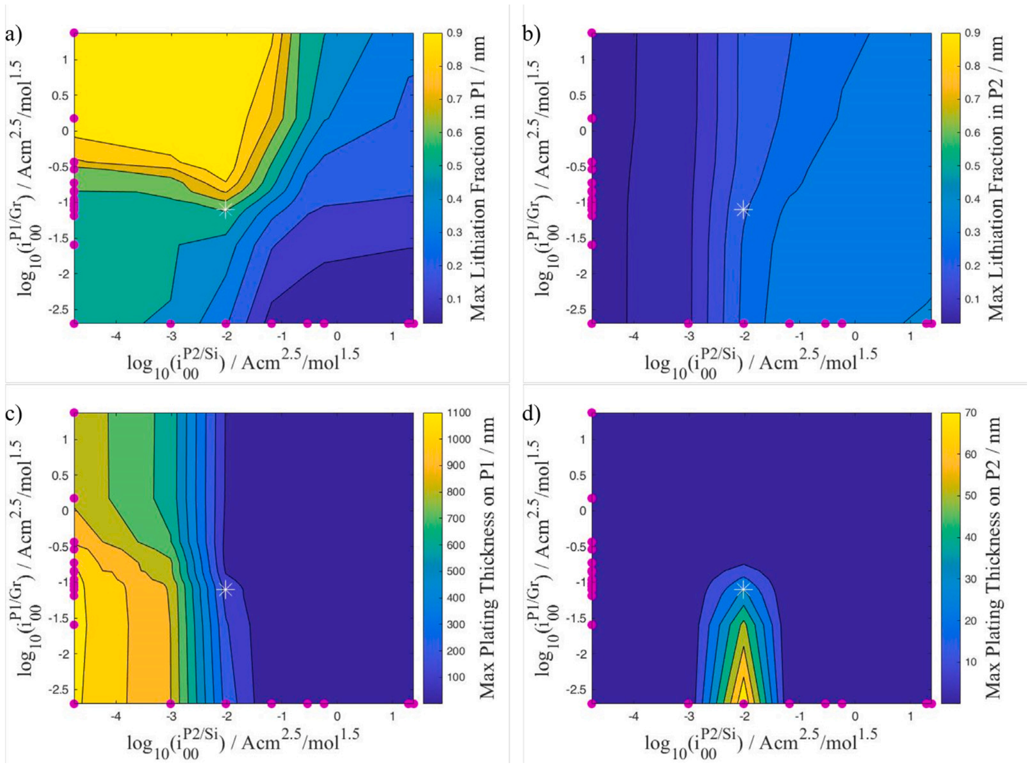

**Fig. 6.** Simulation results of 1 C lithiation of the model half-cell geometry for varying $i_{00}^{\mathrm{mat}}$ (pink dots) as in Table 3 for P1 (representing graphite) in the left column and P2 (representing Si) in the right column: (a) and (b) maximal lithiation fractions and (c) and (d) maximal plating thickness after 1000 s. The asterisk marks the combination of parameters used in simulations with the complex microstructure.

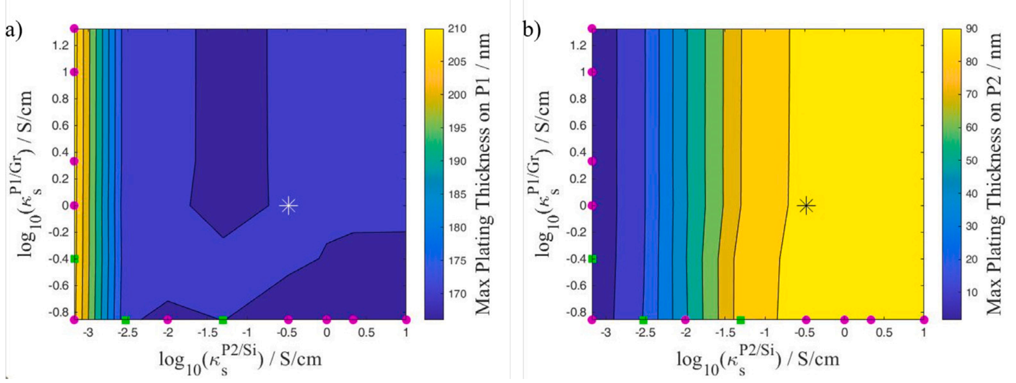

**Fig. 7.** Simulation results of 1 C lithiation of model half-cell geometry for varying $\kappa_s^{mat}$. Pink dots represent reported values in Table 4 and green squares represent additional auxiliary data points in the parameter space: Maximal plating thickness over the whole electrode for (a) P1 (representing graphite) and (b) P2 (representing Si) for all input value combinations after 3600 s. The asterisk marks the combination of parameters used in simulations with the complex microstructure.

Faster intercalation kinetics of graphite compared to Si tend to favor plating on the surface of graphite particles.

### 3.1.4. Electronic conductivity

The results of the parameter study investigating the influence of electronic conductivity on plating consisting of 48 lithiation simulations are presented in Fig. 7. This Figure shows the maximal plating thickness after 1 h of 1 C lithiation (a) on the surface of P1 and (b) on the surface of P2. In general, the influence of conductivity is lower compared to the parameters discussed above. Still, we observe that the plating is more pronounced on the particles with the higher conductivity. In case of conductivities in the order of 1 S/cm, the conductivity has a negligible influence on the distribution of plating on one particle or the other. Only for very low conductivities of P2 we observe a strong increase of plating thickness on P1. Overpotentials drive preferential lithiation of graphite resulting in higher plating thickness (see Supplementary Material). Note that typically Si particles are of smaller size than in the study presented here and/or embedded in a carbon matrix. Therefore the influence of electronic conductivity can be neglected in practical applications.

In conclusion, lower conductivities of Si materials compared to graphite tend to favor plating on graphite particles. Generally, the impact is minor and we do not expect a significant impact of this parameter in realistic electrode microstructures additionally including conductive additives.

### 3.1.5. Adjusted model setup

In Sections 3.1.1 to 3.1.4, we provided an overview on the effect of different material parameters. Finally, we perform a simulation using the input parameters as in the simulations with complex electrode geometry (cf. Table 5). Additionally, we employ the adjusted model setup (cf. Fig. 2(b)) with particle sizes as observed in the tomography data of the LG INR21700-M50T anode. Fig. 8 shows the maximal and minimal lithiation fraction and plating thickness of the two particles during the lithiation simulation with 1 C rate. The lithiation process was discussed in detail in Section 3.1.1. The Si particle is lithiated preferentially in the beginning [17,18,20,26,29,49,50,53]. With increasing state of lithiation the OCP of Si decreases and graphite lithiates preferentially, especially in the two lower voltage plateaus of the graphite OCP. Based on the discussion of the previous sections, we expect more plating on graphite than on Si. Fig. 8 confirms expected trends. In fact, in our simulation using the adjusted model geometry we observe close to no plating on the Si particle. Note that due to the smaller size of the Si particle compared to P2 in previous sections the 1 C rate corresponds to only one fifth of the current density in these simulations.

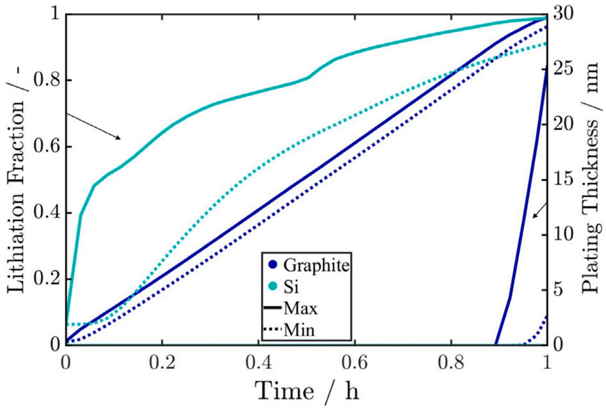

**Fig. 8.** 1C lithiation simulation results employing a model geometry with unequally sized particles: Maximum and minimum lithiation fraction and plating thickness of graphite and Si during 1 h of lithiation. Note that the lithiation fractions are depicted rather in the upper left-hand side of the graph while the plating thickness is apparent at the right-hand side and the plating thickness of Si remains close to zero.

## 3.2. Complex electrode microstructure

After the discussion of the impact of individual material parameters on the distribution and thickness of plating on single particles, we investigate in this section plating in a complex composite electrode microstructure of state-of-the-art commercial anode material. Fig. 9(a) shows the distribution of the lithiation fraction in graphite and Si throughout the thickness of the electrode at the end of a 1 C (6.5 mA/cm$^2$) lithiation simulation. For the high-energy electrode design, 1 C is demanding and we observe a steep gradient of the Li fraction across the electrode at the end of the simulation. The corresponding distribution of plated Li is shown in Fig. 9(b). We observe significant plating in a small layer close to the separator which is consistent with previous reports. At this high C-rate, we reach the onset of plating at only 5.1 % SOC which is similar to values reported in [19]. After reaching this onset, we simulate the lithiation of additional 0.15 mAh/cm$^2$ charge. Fig. 10 shows the maximal lithiation fractions and plating thickness of Si and graphite during this lithiation simulation. In general, trends of the lithiation of the two materials are similar as in the adjusted model geometry. In agreement with the simulations using the model setup, we see a preferential plating of Li on graphite. However, in contrast to the model geometry we also observe plating on Si, although to a minor extent compared to plating on graphite.

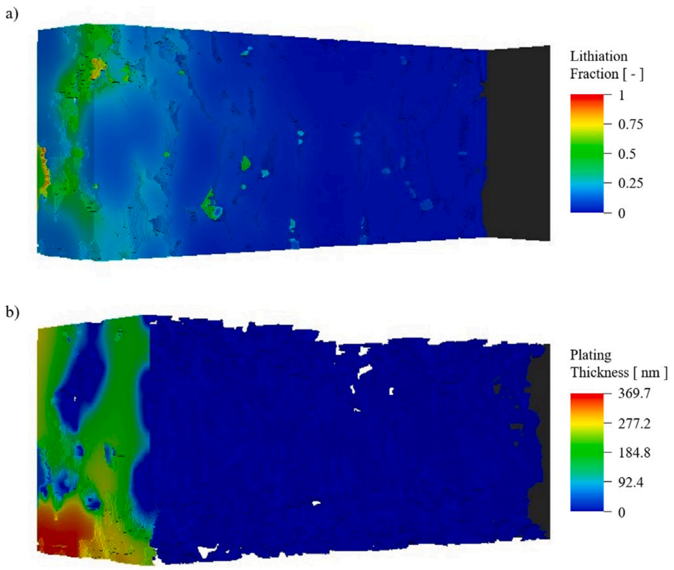

**Fig. 9.** Simulation results of a half-cell using the reconstruction of a state-of-the-art composite anode from an LG INR21700-M50T cell: Spatial distribution of (a) lithiation fractions in a cross section of the electrode and (b) plating thickness in the whole electrode after 222.65 s of 1 C lithiation. A more detailed depiction separating graphite and Si can be found in Fig. S7.

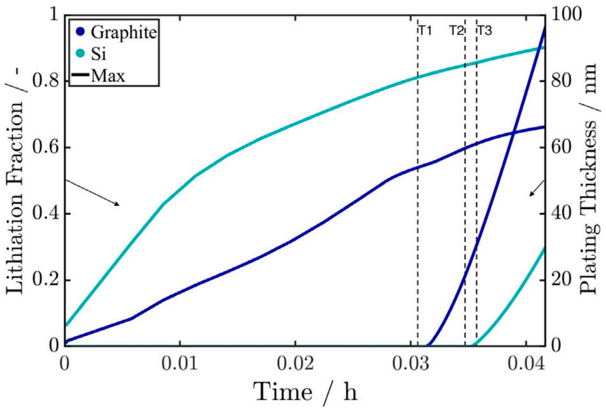

**Fig. 10.** Simulation results of a half-cell using the reconstruction of a state-of-the-art composite anode from an LG INR21700-M50T cell: Maximum lithiation fraction and plating thickness of the active materials graphite and Si during the first 150 s of 1 C lithiation. For the highlighted points in time further analysis is conducted.

To gain more insights into the lithiation and plating behavior of the two active materials, we take a closer look at the time points T1 at 0.0306 h, T2 at 0.0347 h, and T3 at 0.0357 h (highlighted in Fig. 10). T1 is right before the onset of plating, T2 after the onset of plating on graphite but before the onset of plating on Si, and T3 after the onset of plating on both active materials. Applying a blue color scale for graphite and a green color scale for Si, Fig. 11 shows the solid-electrolyte potential difference, the plating thickness, and the relative Faradaic current, $i^{\text{mat}}/(F \cdot c^{\text{mat},max})$, for electrode areas relevant to plating analysis. Fig. 11(a), (d), and (g) show the potential difference between the solid phase and the electrolyte $\phi_s^{\text{mat}} - \varphi_e$ at the surface of Si and graphite particles. While the differences in the electric potential of the solid phases within the layers perpendicular to the through direction are very small, the electrochemical potential of the electrolyte phase exhibits significant gradients depicted in Fig. S8. At T1, the plating condition $\phi_s^{\text{mat}} - \varphi_e \leq 0$ is met first at the graphite surface at the lower left corner of the microstructure. In this region, we also observe prominent Li plating at times larger T1 as shown in Fig. 11(b), (e), and (h). Since local differences in the plating overpotential are mainly due to fluctuations in the electrolyte potential, it is instructive to have a closer look at the local Faradaic current which is shown in Fig. 11(c), (f), and (i). Due to the preferred lithiation of Si in the beginning of the simulation (cf. Fig. 10), at times larger T1 mostly graphite is electrochemically active close to the separator. Therefore, the Faradaic current and the corresponding potential difference is much larger on the graphite surface. The resulting changes in current distribution and electrolyte potential favor Li deposition on graphite. This underlines the complex interactions of the two materials discussed on the example of our model system. Microstructural features affecting reaction and transport processes in the electrode further enhance such features in realistic electrode geometries.

*Effect of C-rate.* Additionally, we performed simulations with decreasing C-rates. To ensure comparable results, we terminate the lithiation process in all cases after transferring 0.15 mAh/cm$^2$ of charge beyond the onset of Li plating. Fig. 12 shows a summary of simulation results of the C-rate test. As expected, the cell voltage and capacity decrease with increasing C-rate. The average plating thickness in the electrode included as dashed line in the graph is highest at 1 C and of comparable magnitude at lower currents. Fig. 13 shows corresponding depth profiles of plating thickness and normalized Li concentration for both materials. The interface to the separator is at 0 μm depth. Fig. 13(a) reveals that close to the separator the plating thickness is highest at all currents. Generally, the mean plating thickness on graphite is higher close to the separator. Further into the electrode, we observe more plating on Si compared to graphite. Note that the plating depth increases with C-rate, though this effect is only marginal. Therefore, high resolution imaging of the volume close to the surface is important to accurately predict Li plating. Fig. 13(b) shows the lithiation fraction of the two materials. Utilization of the electrodes decreases with increasing C-rate. The lithiation fraction at the separator is in all cases close to 1. Only at 1 C graphite utilization drops to around 70 % at the surface [57]. Note that for the lowest applied C-rate plating did not start before an SOC of 90.1 %, which would not have been reached in a full-cell with typical electrode balancing.

## 4. Conclusions

3D microstructure-resolved simulations provide a comprehensive understanding of the relevant factors for Li plating in Si/graphite composite electrodes. A parameter study was performed on a model half-cell geometry to study the effect of material parameters. In our study, we investigate the effect of the chemical diffusion constant of Li in the active material, the electronic conductivity, the open-circuit potential, and the rate constant of the Faradaic reaction. The range of parameters was determined based on a comprehensive screening of the existing literature. Simulations have shown that the chemical diffusion coefficient, rate constant, and OCP have a significant impact on Li plating, whereas the effect of electric conductivity is generally minor. A relevant factor is the complex interaction of parameters in the simulation which influence the distribution of current and plating accordingly. The parameter study shows that the generally higher OCP of Si-containing electrodes is not the major factor reducing the risk of lithium plating. However, the parameter study suggests that for typical material parameters of the OCP, intercalation rate, and conductivity plating tends to occur preferentially on graphite particles. Only low chemical diffusion of lithium in Si particles favors plating on the Si surface.

Finally, we perform simulations on a reconstruction of state-of-the-art commercial anode material. Already at moderate C-rates we found significant plating on graphite and Si particles close to the separator. Analysis of potential and current distributions at the surface of graphite and Si particles suggests that preferential lithiation of graphite in the critical stage of the charging process is causing plating on graphite

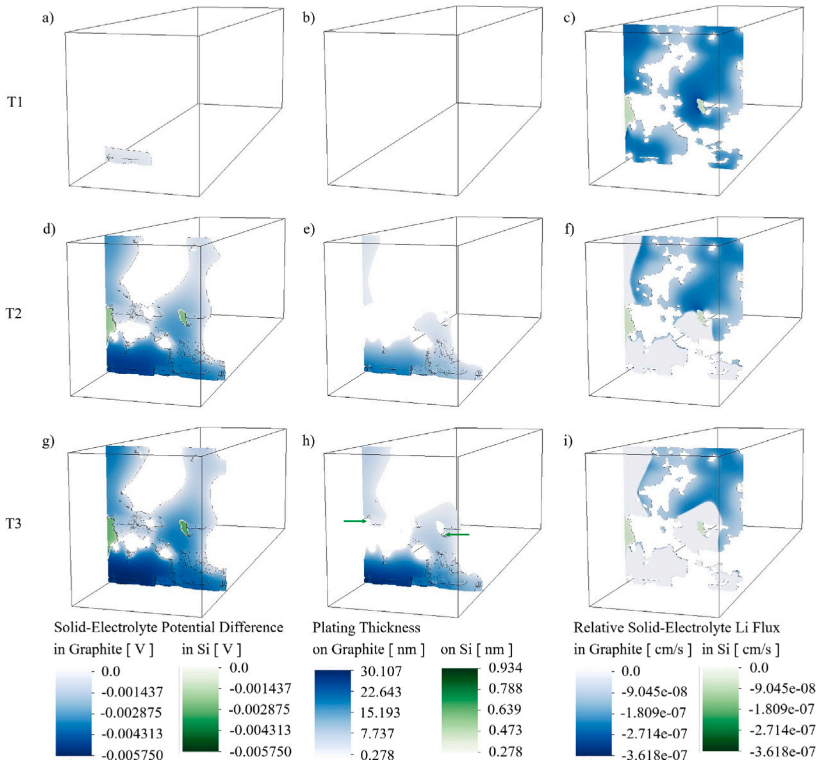

**Fig. 11.** Simulation results of a half-cell using the reconstruction of a state-of-the-art composite anode from an LG INR21700-M50T cell: Spatial distribution of (a), (d), and (g) the solid-electrolyte potential difference, (b), (e), and (h) the plating thickness, and (c), (f), and (i) the relative solid-electrolyte Li flux after 0.0306 h (T1), 0.0347 h (T2), and 0.0357 h (T3) of 1 C lithiation. In (a), (d), and (g) only voxels with $\phi_s^{\mathrm{mat}} - \varphi_e \leq 0$ are depicted, in (b), (e), and (h) only Li depositions above one mono-layer, and in (c), (f), and (i) only the surface layers of the electrode to enable a precise representation.

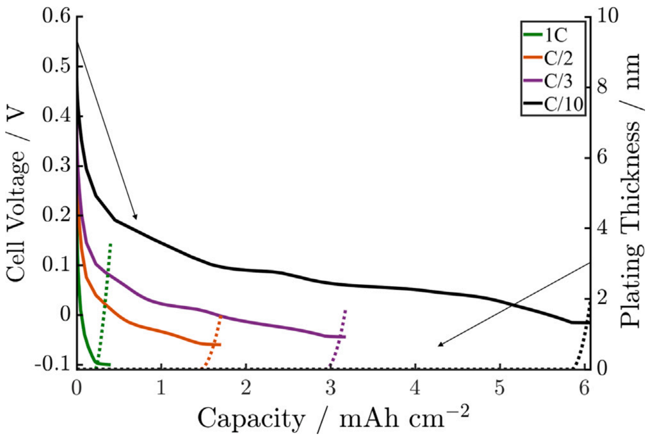

**Fig. 12.** Simulation results of a half-cell using the reconstruction of a state-of-the-art composite anode from an LG INR21700-M50T cell: Cell voltage (solid lines) and plating thickness (dotted lines) in the whole electrode during the lithiation with varying C-rates.

surfaces. In contrast to the model geometries, plating was also found on the surface of Si particles, though plating on Si is delayed compared to plating on graphite.

Our study shows that adding Si per se does not guarantee a reduction of the risk of lithium plating from a materials perspective. Still, the high specific capacity of Si materials is able to significantly reduce electrode thickness at the same areal capacity. This effect reduces transport limitations and mitigates the tendency of Li plating. However, desirable are significantly higher Si contents compared to state-of-the-art electrodes investigated in this work. In this case, detailed simulation studies on the effect of structural changes due to volume expansion of the Si material on fast charging and plating are still lacking and will be subject to future work.

## CRediT authorship contribution statement

**Lioba Boveleth:** Writing – original draft, Visualization, Methodology, Investigation, Conceptualization. **Adrian Lindner:** Writing – original draft, Investigation. **Wolfgang Menesklou:** Writing – review & editing, Funding acquisition. **Timo Danner:** Writing – review & editing, Supervision, Project administration, Funding acquisition, Conceptualization. **Arnulf Latz:** Writing – review & editing, Funding acquisition.

## Declaration of competing interest

The authors declare that they have no known competing financial interests or personal relationships that could have appeared to influence the work reported in this paper.

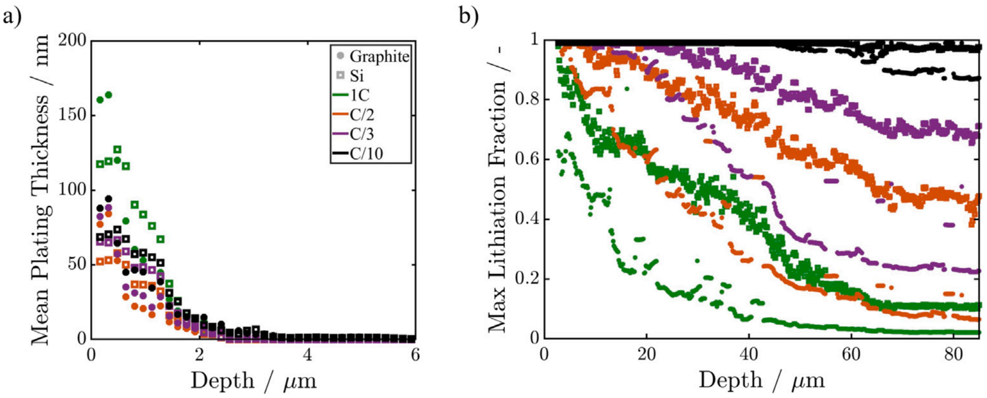

**Fig. 13.** Simulation results of a half-cell using the reconstruction of a state-of-the-art composite anode from an LG INR21700-M50T cell: (a) mean plating thickness and (b) maximum lithiation fraction in every slice of voxels across the thickness of the electrode at the end of the lithiation with varying C-rates. Closed circles represent graphite material and open squares represent Si. The interface to the separator is at a depth of 0 μm. See Fig. S9 for additional results across the thickness of the electrode.

## Data availability

Data will be made available on request.

## Acknowledgments

The authors would like to thank the German Federal Ministry of Education and Research (BMBF) for the funding of the projects CharLiSiKo (03XP0333C) and MiCha (03XP0317B) managed by Projektträger Jülich (PTJ) and gratefully acknowledge the fruitful discussions with and the ongoing improvement and upgrading of BEST by Simon Hein (DLR). The work performed at DLR contributes to the research at CELEST (Center for Electrochemical Energy Storage Ulm-Karlsruhe). The simulations were carried out on the bwHPC cluster JUSTUS 2 supported by the state of Baden-Württemberg and the German Research Foundation (DFG) through grant No INST 40/575-1 FUGG.

## Appendix A. Supplementary data

Supplementary material related to this article can be found online at https://doi.org/10.1016/j.electacta.2024.145010.

## References

[1] J. Asenbauer, T. Eisenmann, M. Kuenzel, A. Kazzazi, Z. Chen, D. Bresser, The success story of graphite as a lithium-ion anode material – fundamentals, remaining challenges, and recent developments including silicon (oxide) composites, Sustain. Energy Fuels 4 (2020) 5387–5416, http://dx.doi.org/10.1039/D0SE00175A.

[2] J.T. Frith, M.J. Lacey, U. Ulissi, A non-academic perspective on the future of lithium-based batteries, Nature Commun. 14 (420) (2023) http://dx.doi.org/10.1038/s41467-023-35933-2.

[3] R. Chandrasekaran, A. Magasinski, G. Yushin, T.F. Fuller, Analysis of lithium insertion/deinsertion in a silicon electrode particle at room temperature, J. Electrochem. Soc. 157 (10) (2010) A1139, http://dx.doi.org/10.1149/1.3474225.

[4] V.A. Sethuraman, V. Srinivasan, A.F. Bower, P.R. Guduru, In situ measurements of stress-potential coupling in lithiated silicon, J. Electrochem. Soc. 157 (11) (2010) A1253, http://dx.doi.org/10.1149/1.3489378.

[5] Z. Chen, L. Christensen, J. Dahn, Large-volume-change electrodes for Li-ion batteries of amorphous alloy particles held by elastomeric tethers, Electrochem. Commun. 5 (11) (2003) 919–923, http://dx.doi.org/10.1016/j.elecom.2003.08.017.

[6] M. Yu, E. Temeche, S. Indris, R.M. Laine, Sustainable SiC composite anodes, graphite accelerated lithium storage, J. Electrochem. Soc. 170 (7) (2023) 070504, http://dx.doi.org/10.1149/1945-7111/ace132.

[7] P. Li, H. Kim, S.-T. Myung, Y.-K. Sun, Diverting exploration of silicon anode into practical way: A review focused on silicon-graphite composite for lithium ion batteries, Energy Storage Mater. 35 (2021) 550–576, http://dx.doi.org/10.1016/j.ensm.2020.11.028.

[8] S. Chae, S.-H. Choi, N. Kim, J. Sung, J. Cho, Integration of graphite and silicon anodes for the commercialization of high-energy lithium-ion batteries, Angew. Chem. Int. Ed. 59 (1) (2020) 110–135, http://dx.doi.org/10.1002/anie.201902085.

[9] T. Waldmann, B.-I. Hogg, M. Wohlfahrt-Mehrens, Li plating as unwanted side reaction in commercial Li-ion cells – A review, J. Power Sources 384 (2018) 107–124, http://dx.doi.org/10.1016/j.jpowsour.2018.02.063.

[10] S. Hein, A. Latz, Influence of local lithium metal deposition in 3D microstructures on local and global behavior of lithium-ion batteries, Electrochim. Acta 201 (2016) 354–365, http://dx.doi.org/10.1016/j.electacta.2016.01.220.

[11] M. Petzl, M.A. Danzer, Nondestructive detection, characterization, and quantification of lithium plating in commercial lithium-ion batteries, J. Power Sources 254 (2014) 80–87, http://dx.doi.org/10.1016/j.jpowsour.2013.12.060.

[12] X.-G. Yang, Y. Leng, G. Zhang, S. Ge, C.-Y. Wang, Modeling of lithium plating induced aging of lithium-ion batteries: Transition from linear to nonlinear aging, J. Power Sources 360 (2017) 28–40, http://dx.doi.org/10.1016/j.jpowsour.2017.05.110.

[13] H. Zhang, J. Chen, G. Zeng, X. Wu, J. Wang, J. Xue, Y.-h. Hong, Y. Qiao, S.-G. Sun, Quantifying the influence of Li plating on a graphite anode by mass spectrometry, Nano Lett. 23 (8) (2023) 3565–3572, http://dx.doi.org/10.1021/acs.nanolett.3c00729, PMID: 37026665.

[14] C. Weisenberger, D.K. Harrison, C. Zhou, V. Knoblauch, Revealing the effects of microstructural changes of graphite anodes during cycling on their lithium intercalation kinetics utilizing operando XRD, Electrochim. Acta 461 (2023) 142629, http://dx.doi.org/10.1016/j.electacta.2023.142629.

[15] M. Flügel, M. Bolsinger, M. Marinaro, V. Knoblauch, M. Hölzle, M. Wohlfahrt-Mehrens, T. Waldmann, Onset shift of Li plating on Si/Graphite anodes with increasing Si content, J. Electrochem. Soc. 170 (6) (2023) 060536, http://dx.doi.org/10.1149/1945-7111/acdda3.

[16] Z. Yang, S.E. Trask, X. Wu, B.J. Ingram, Effect of Si content on extreme fast charging behavior in silicon - graphite composite anodes, Batteries 9 (2) (2023) http://dx.doi.org/10.3390/batteries9020138.

[17] Y. Chen, F. Guo, L. Yang, J. Lu, D. Liu, H. Wang, J. Zheng, X. Yu, H. Li, Probing component contributions and internal polarization in silicon-graphite composite anode for lithium-ion batteries with an electrochemical-mechanical model, Chin. Phys. B 31 (7) (2022) 078201, http://dx.doi.org/10.1088/1674-1056/ac6012.

[18] J. Tao, L. Liu, J. Han, J. Peng, Y. Chen, Y. Yang, H. rong Yao, J. Li, Z. Huang, Y. Lin, New perspectives on spatial dynamics of lithiation and lithium plating in graphite/silicon composite anodes, Energy Storage Mater. 60 (2023) 102809, http://dx.doi.org/10.1016/j.ensm.2023.102809.

[19] V. Kabra, M. Parmananda, C. Fear, F.L.E. Usseglio-Viretta, A. Colclasure, K. Smith, P.P. Mukherjee, Mechanistic analysis of microstructural attributes to lithium plating in fast charging, ACS Appl. Mater. Interfaces 12 (50) (2020) 55795–55808, http://dx.doi.org/10.1021/acsami.0c15144, PMID: 33274910.

[20] X. Gao, S. Li, J. Xue, D. Hu, J. Xu, A mechanistic and quantitative understanding of the interactions between SiO and graphite particles, Adv. Energy Mater. 13 (2) (2023) 2202584, http://dx.doi.org/10.1002/aenm.202202584.

[21] C. Liu, O. Arcelus, T. Lombardo, H. Oularbi, A.A. Franco, Towards a 3D-resolved model of Si/Graphite composite electrodes from manufacturing simulations, J. Power Sources 512 (2021) 230486, http://dx.doi.org/10.1016/j.jpowsour.2021.230486.

[22] E. Hosseinzadeh, J. Marco, P. Jennings, Electrochemical-thermal modelling and optimisation of lithium-ion battery design parameters using analysis of variance, Energies 10 (9) (2017) http://dx.doi.org/10.3390/en10091278.

[23] Q. Lai, S. Jangra, H.J. Ahn, G. Kim, W.T. Joe, X. Lin, Analytical sensitivity analysis for battery electrochemical parameters, in: 2019 American Control Conference, ACC, 2019, pp. 890–896, http://dx.doi.org/10.23919/ACC.2019.8814950.

[24] W. Li, D. Cao, D. Jöst, F. Ringbeck, M. Kuipers, F. Frie, D.U. Sauer, Parameter sensitivity analysis of electrochemical model-based battery management systems for lithium-ion batteries, Appl. Energy 269 (2020) 115104, http://dx.doi.org/10.1016/j.apenergy.2020.115104.

[25] M. Andersson, M. Streb, J.Y. Ko, V. Löfqvist Klass, M. Klett, H. Ekström, M. Johansson, G. Lindbergh, Parametrization of physics-based battery models from input–output data: A review of methodology and current research, J. Power Sources 521 (2022) 230859, http://dx.doi.org/10.1016/j.jpowsour.2021.230859.

[26] D.J. Pereira, A.M. Aleman, J.W. Weidner, T.R. Garrick, A mechano-electrochemical battery model that accounts for preferential lithiation inside blended silicon graphite (Si/C) anodes, J. Electrochem. Soc. 169 (2) (2022) 020577, http://dx.doi.org/10.1149/1945-7111/ac554f.

[27] B. Liu, Y. Jia, J. Li, H. Jiang, S. Yin, J. Xu, Multiphysics coupled computational model for commercialized Si/graphite composite anode, J. Power Sources 450 (2020) 227667, http://dx.doi.org/10.1016/j.jpowsour.2019.227667.

[28] X. Gao, W. Lu, J. Xu, Modeling framework for multiphysics-multiscale behavior of Si–C composite anode, J. Power Sources 449 (2020) 227501, http://dx.doi.org/10.1016/j.jpowsour.2019.227501.

[29] P.-F. Lory, B. Mathieu, S. Genies, Y. Reynier, A. Boulineau, W. Hong, M. Chandesris, Probing silicon lithiation in silicon-carbon blended anodes with a multi-scale porous electrode model, J. Electrochem. Soc. 167 (12) (2020) 120506, http://dx.doi.org/10.1149/1945-7111/abaa69.

[30] S. Dhillon, G. Hernández, N.P. Wagner, A.M. Svensson, D. Brandell, Modelling capacity fade in silicon-graphite composite electrodes for lithium-ion batteries, Electrochim. Acta 377 (2021) 138067, http://dx.doi.org/10.1016/j.electacta.2021.138067.

[31] X. Gao, W. Lu, J. Xu, Insights into the Li diffusion mechanism in Si/C composite anodes for lithium-ion batteries, ACS Appl. Mater. Interfaces 13 (18) (2021) 21362–21370, http://dx.doi.org/10.1021/acsami.1c03366.

[32] W. Ai, N. Kirkaldy, Y. Jiang, G. Offer, H. Wang, B. Wu, A composite electrode model for lithium-ion batteries with silicon/graphite negative electrodes, J. Power Sources 527 (2022) 231142, http://dx.doi.org/10.1016/j.jpowsour.2022.231142.

[33] Y. Jiang, Z. Niu, G. Offer, J. Xuan, H. Wang, Insights into the role of silicon and graphite in the electrochemical performance of silicon/graphite blended electrodes with a multi-material porous electrode model, J. Electrochem. Soc. 169 (2) (2022) 020568, http://dx.doi.org/10.1149/1945-7111/ac5481.

[34] T. Boivin, B. Mathieu, W. Porcher, O. Gillia, Breathing of a silicon-based anode: Mechanical discrete approach using DEM, J. Electrochem. Soc. 171 (1) (2024) 010505, http://dx.doi.org/10.1149/1945-7111/ad14cf.

[35] J.S. Edge, S. O'Kane, R. Prosser, N.D. Kirkaldy, A.N. Patel, A. Hales, A. Ghosh, W. Ai, J. Chen, J. Yang, S. Li, M.-C. Pang, L. Bravo Diaz, A. Tomaszewska, M.W. Marzook, K.N. Radhakrishnan, H. Wang, Y. Patel, B. Wu, G.J. Offer, Lithium ion battery degradation: what you need to know, Phys. Chem. Chem. Phys. 23 (2021) 8200–8221, http://dx.doi.org/10.1039/D1CP00359C.

[36] M. Flügel, K. Richter, M. Wohlfahrt-Mehrens, T. Waldmann, Detection of Li deposition on Si/Graphite anodes from commercial Li-ion cells: A post-mortem GD-OES depth profiling study, J. Electrochem. Soc. 169 (5) (2022) 050533, http://dx.doi.org/10.1149/1945-7111/ac70af.

[37] S. Ding, Y. Li, H. Dai, L. Wang, X. He, Accurate model parameter identification to boost precise aging prediction of lithium-ion batteries: A review, Adv. Energy Mater. 13 (39) (2023) 2301452, http://dx.doi.org/10.1002/aenm.202301452.

[38] I. Pivarníková, M. Flügel, N. Paul, A. Cannavo, G. Ceccio, J. Vacík, P. Müller-Buschbaum, M. Wohlfahrt-Mehrens, R. Gilles, T. Waldmann, Observation of preferential sputtering of Si/graphite anodes from Li-ion cells by GD-OES and its validation by neutron depth profiling, J. Power Sources 594 (2024) 233972, http://dx.doi.org/10.1016/j.jpowsour.2023.233972.

[39] X. Lu, M. Lagnoni, A. Bertei, S. Das, R.E. Owen, Q. Li, K. O'Regan, A. Wade, D.P. Finegan, E. Kendrick, M.Z. Bazant, D.J.L. Brett, P.R. Shearing, Multiscale dynamics of charging and plating in graphite electrodes coupling operando microscopy and phase-field modelling, Nature Commun. 14 (2023) http://dx.doi.org/10.1038/s41467-023-40574-6.

[40] P. Arora, M. Doyle, R.E. White, Mathematical modeling of the lithium deposition overcharge reaction in lithium-ion batteries using carbon-based negative electrodes, J. Electrochem. Soc. 146 (10) (1999) 3543, http://dx.doi.org/10.1149/1.1392512.

[41] S. Hein, T. Danner, A. Latz, An electrochemical model of lithium plating and stripping in lithium ion batteries, ACS Appl. Energy Mater. 3 (9) (2020) 8519–8531, http://dx.doi.org/10.1021/acsaem.0c01155.

[42] R. Fang, C.P. Schmidt, W.A. Wall, A coupled finite element approach to spatially resolved lithium plating and stripping in three-dimensional anode microstructures of lithium-ion cells, J. Comput. Phys. 461 (2022) 111179, http://dx.doi.org/10.1016/j.jcp.2022.111179.

[43] P. Brodsky Ringler, M. Wise, P. Ramesh, J.H. Kim, M. Canova, C. Bae, J. Deng, H. Park, Modeling of lithium plating and stripping dynamics during fast charging, Batteries 9 (7) (2023) http://dx.doi.org/10.3390/batteries9070337.

[44] Z. He, H. Li, W. Ji, W. Li, Y. Zhang, X. Li, P. Zhang, J. Zhao, Investigation on Li-plating prevention optimal charging protocol of nickel-rich/graphite-SiOx lithium ion battery, J. Power Sources 571 (2023) 233044, http://dx.doi.org/10.1016/j.jpowsour.2023.233044.

[45] C.-H. Chen, F.B. Planella, K. O'Regan, D. Gastol, W.D. Widanage, E. Kendrick, Development of experimental techniques for parameterization of multi-scale lithium-ion battery models, J. Electrochem. Soc. 167 (2020) 080534, http://dx.doi.org/10.1149/1945-7111/ab9050.

[46] V. De Lauri, L. Krumbein, S. Hein, B. Prifling, V. Schmidt, T. Danner, A. Latz, Beneficial effects of three-dimensional structured electrodes for the fast charging of lithium-ion batteries, ACS Appl. Energy Mater. 4 (12) (2021) 13847–13859, http://dx.doi.org/10.1021/acsaem.1c02621.

[47] A. Latz, J. Zausch, Thermodynamic consistent transport theory of Li-ion batteries, J. Power Sources 196 (6) (2011) 3296–3302, http://dx.doi.org/10.1016/j.jpowsour.2010.11.088.

[48] T. Knorr, S. Hein, B. Prifling, M. Neumann, T. Danner, V. Schmidt, A. Latz, Simulation-based and data-driven techniques for quantifying the influence of the carbon binder domain on electrochemical properties of Li-ion batteries, Energies 15 (21) (2022) http://dx.doi.org/10.3390/en15217821.

[49] J. Park, S.S. Park, Y.S. Won, In situ XRD study of the structural changes of graphite anodes mixed with SiOx during lithium insertion and extraction in lithium ion batteries, Electrochim. Acta 107 (2013) 467–472, http://dx.doi.org/10.1016/j.electacta.2013.06.059.

[50] K.P.C. Yao, J.S. Okasinski, K. Kalaga, J.D. Almer, D.P. Abraham, Operando quantification of (de)lithiation behavior of silicon–graphite blended electrodes for lithium-ion batteries, Adv. Energy Mater. 9 (8) (2019) 1803380, http://dx.doi.org/10.1002/aenm.201803380.

[51] C. Heubner, T. Liebmann, O. Lohrberg, S. Cangaz, S. Maletti, A. Michaelis, Understanding component-specific contributions and internal dynamics in silicon/graphite blended electrodes for high-energy lithium-ion batteries, Batter. Supercaps 5 (1) (2022) e202100182, http://dx.doi.org/10.1002/batt.202100182.

[52] A.A. Wang, S.E.J. O'Kane, F.B. Planella, J.L. Houx, K. O'Regan, M. Zyskin, J. Edge, C.W. Monroe, S.J. Cooper, D.A. Howey, E. Kendrick, J.M. Foster, Review of parameterisation and a novel database (LiionDB) for continuum Li-ion battery models, Prog. Energy 4 (3) (2022) 032004, http://dx.doi.org/10.1088/2516-1083/ac692c.

[53] C. Hogrefe, N. Paul, L. Boveleth, M. Bolsinger, M. Flügel, T. Danner, A. Latz, R. Gilles, V. Knoblauch, M. Wohlfahrt-Mehrens, M. Hölzle, T. Waldmann, Lithium redistribution mechanism within silicon-graphite electrodes: Multi-method approach and method validation, J. Electrochem. Soc. 171 (7) (2024) 070503, http://dx.doi.org/10.1149/1945-7111/ad59c7.

[54] Y. Jiang, G. Offer, J. Jiang, M. Marinescu, H. Wang, Voltage hysteresis model for silicon electrodes for lithium ion batteries, including multi-step phase transformations, crystallization and amorphization, J. Electrochem. Soc. 167 (13) (2020) 130533, http://dx.doi.org/10.1149/1945-7111/abbbba.

[55] D. Wycisk, M. Oldenburger, M.G. Stoye, T. Mrkonjic, A. Latz, Modified plett-model for modeling voltage hysteresis in lithium-ion cells, J. Energy Storage 52 (2022) 105016, http://dx.doi.org/10.1016/j.est.2022.105016.

[56] Y. Gao, Z. Sun, D. Zhang, D. Shi, X. Zhang, Determination of half-cell open-circuit potential curve of silicon-graphite in a physics-based model for lithium-ion batteries, Appl. Energy 349 (2023) 121621, http://dx.doi.org/10.1016/j.apenergy.2023.121621.

[57] J. Knorr, A. Gomez-Martin, H.-C. Hsiao, A. Adam, B. Rödl, M.A. Danzer, Effect of different charge rates on the active material lithiation of Gr/SiOx blend anodes in lithium-ion cells, J. Energy Storage 86 (2024) 111151, http://dx.doi.org/10.1016/j.est.2024.111151.

[58] N. Ding, J. Xu, Y. Yao, G. Wegner, X. Fang, C. Chen, I. Lieberwirth, Determination of the diffusion coefficient of lithium ions in nano-Si, Solid State Ion. 180 (2) (2009) 222–225, http://dx.doi.org/10.1016/j.ssi.2008.12.015.

[59] L. von Kolzenberg, A. Latz, B. Horstmann, Chemo-mechanical model of SEI growth on silicon electrode particles, Batter. Supercaps 5 (2) (2022) e202100216, http://dx.doi.org/10.1002/batt.202100216.

[60] K. Pan, F. Zou, M. Canova, Y. Zhu, J.-H. Kim, Systematic electrochemical characterizations of Si and SiO anodes for high-capacity Li-ion batteries, J. Power Sources 413 (2019) 20–28, http://dx.doi.org/10.1016/j.jpowsour.2018.12.010.

[61] L. Köbbing, A. Latz, B. Horstmann, Voltage hysteresis of silicon nanoparticles: Chemo-mechanical particle-SEI model, Adv. Funct. Mater. 34 (7) (2024) 2308818, http://dx.doi.org/10.1002/adfm.202308818.

[62] J. Sturm, A. Rheinfeld, I. Zilberman, F. Spingler, S. Kosch, F. Frie, A. Jossen, Modeling and simulation of inhomogeneities in a 18650 nickel-rich, silicon-graphite lithium-ion cell during fast charging, J. Power Sources 412 (2019) 204–223, http://dx.doi.org/10.1016/j.jpowsour.2018.11.043.

[63] M. Park, X. Zhang, M. Chung, G.B. Less, A.M. Sastry, A review of conduction phenomena in Li-ion batteries, J. Power Sources 195 (24) (2010) 7904–7929, http://dx.doi.org/10.1016/j.jpowsour.2010.06.060.

[64] M.D. Levi, E. Markevich, D. Aurbach, The effect of slow interfacial kinetics on the chronoamperometric response of composite lithiated graphite electrodes and on the calculation of the chemical diffusion coefficient of Li ions in graphite, J. Phys. Chem. B 109 (15) (2005) 7420–7427, http://dx.doi.org/10.1021/jp0441902, PMID: 16851850.

[65] S. Zhang, K. Xu, T. Jow, Low temperature performance of graphite electrode in Li-ion cells, Electrochim. Acta 48 (3) (2002) 241–246, http://dx.doi.org/10.1016/S0013-4686(02)00620-5.

[66] Z. Chen, D.L. Danilov, Q. Zhang, M. Jiang, J. Zhou, R.-A. Eichel, P.H. Notten, Modeling NCA/C6-Si battery ageing, Electrochim. Acta 430 (2022) 141077, http://dx.doi.org/10.1016/j.electacta.2022.141077.

[67] V. Srinivasan, J. Newman, Design and optimization of a natural graphite/iron phosphate lithium-ion cell, J. Electrochem. Soc. 151 (10) (2004) A1530, http://dx.doi.org/10.1149/1.1785013.

[68] G.-H. Kim, K. Smith, K.-J. Lee, S. Santhanagopalan, A. Pesaran, Multi-domain modeling of lithium-ion batteries encompassing multi-physics in varied length scales, J. Electrochem. Soc. 158 (8) (2011) A955, http://dx.doi.org/10.1149/1.3597614.

[69] P. Johari, Y. Qi, V.B. Shenoy, The mixing mechanism during lithiation of Si negative electrode in Li-ion batteries: An ab initio molecular dynamics study, Am. Chem. Soc. 11 (2011) http://dx.doi.org/10.1021/nl203302d.

[70] Z. Chen, D.L. Danilov, L.H. Raijmakers, K. Chayambuka, M. Jiang, L. Zhou, J. Zhou, R.-A. Eichel, P.H. Notten, Overpotential analysis of graphite-based Li-ion batteries seen from a porous electrode modeling perspective, J. Power Sources 509 (2021) 230345, http://dx.doi.org/10.1016/j.jpowsour.2021.230345.

[71] K. Yoshimura, J. Suzuki, K. Sekine, T. Takamura, Measurement of the diffusion rate of Li in silicon by the use of bipolar cells, J. Power Sources 174 (2) (2007) 653–657, http://dx.doi.org/10.1016/j.jpowsour.2007.06.115.

[72] M. Wang, X. Xiao, X. Huang, Study of lithium diffusivity in amorphous silicon via finite element analysis, J. Power Sources 307 (2016) 77–85, http://dx.doi.org/10.1016/j.jpowsour.2015.12.082.

[73] M. Doyle, Y. Fuentes, Computer simulations of a lithium-ion polymer battery and implications for higher capacity next-generation battery designs, J. Electrochem. Soc. 150 (6) (2003) A706, http://dx.doi.org/10.1149/1.1569478.

[74] M. Doyle, J. Newman, A.S. Gozdz, C.N. Schmutz, J.-M. Tarascon, Comparison of modeling predictions with experimental data from plastic lithium ion cells, J. Electrochem. Soc. 143 (6) (1996) 1890–1903, http://dx.doi.org/10.1149/1.1836921.

[75] L. Cai, R.E. White, Reduction of model order based on proper orthogonal decomposition for lithium-ion battery simulations, J. Electrochem. Soc. 156 (3) (2009) A154, http://dx.doi.org/10.1149/1.3049347.

[76] M. Pharr, K. Zhao, X. Wang, Z. Suo, J.J. Vlassak, Kinetics of initial lithiation of crystalline silicon electrodes of lithium-ion batteries, Nano Lett. 12 (9) (2012) 5039–5047, http://dx.doi.org/10.1021/nl302841y, PMID: 22889293.

[77] E. Martínez-Rosas, R. Vasquez-Medrano, A. Flores-Tlacuahuac, Modeling and simulation of lithium-ion batteries, Comput. Chem. Eng. 35 (9) (2011) 1937–1948, http://dx.doi.org/10.1016/j.compchemeng.2011.05.007.

[78] V.R. Subramanian, V. Boovaragavan, V.D. Diwakar, Toward real-time simulation of physics based lithium-ion battery models, Electrochem. Solid-State Lett. 10 (11) (2007) A255, http://dx.doi.org/10.1149/1.2776128.

[79] L.S. Kremer, T. Danner, S. Hein, A. Hoffmann, B. Prifling, V. Schmidt, A. Latz, M. Wohlfahrt-Mehrens, Influence of the electrolyte salt concentration on the rate capability of ultra-thick NCM 622 electrodes, Batter. Supercaps 3 (11) (2020) 1172–1182, http://dx.doi.org/10.1002/batt.202000098.

[80] R. Chandrasekaran, T.F. Fuller, Analysis of the lithium-ion insertion silicon composite electrode/separator/lithium foil cell, J. Electrochem. Soc. 158 (8) (2011) A859, http://dx.doi.org/10.1149/1.3589301.

[81] W. Mai, A. Colclasure, K. Smith, A reformulation of the Pseudo2D battery model coupling large electrochemical-mechanical deformations at particle and electrode levels, J. Electrochem. Soc. 166 (8) (2019) A1330, http://dx.doi.org/10.1149/2.0101908jes.

[82] P. Arora, M. Doyle, A.S. Gozdz, R.E. White, J. Newman, Comparison between computer simulations and experimental data for high-rate discharges of plastic lithium-ion batteries, J. Power Sources 88 (2) (2000) 219–231, http://dx.doi.org/10.1016/S0378-7753(99)00527-3.

[83] M. Safari, C. Delacourt, Modeling of a commercial graphite/LiFePO4 cell, J. Electrochem. Soc. 158 (5) (2011) A562, http://dx.doi.org/10.1149/1.3567007.

[84] A. Verma, A. Franco, P. Mukherjee, Mechanistic elucidation of Si particle morphology on electrode performance, J. Electrochem. Soc. 166 (2019) A3852–A3860, http://dx.doi.org/10.1149/2.0961915jes.

[85] J. Li, X. Xiao, F. Yang, M.W. Verbrugge, Y.-T. Cheng, Potentiostatic intermittent titration technique for electrodes governed by diffusion and interfacial reaction, J. Phys. Chem. C 116 (1) (2012) 1472–1478, http://dx.doi.org/10.1021/jp207919q.

[86] A. Latz, J. Zausch, Multiscale modeling of lithium ion batteries: thermal aspects, Beilstein J. Nanotechnol. 6 (2015) 987–1007, http://dx.doi.org/10.3762/bjnano.6.102.

[87] E.M. Pell, Diffusion rate of Li in Si at low temperatures, Phys. Rev. 119 (1960) 1222–1225, http://dx.doi.org/10.1103/PhysRev.119.1222.

[88] M. Mastali, M. Farkhondeh, S. Farhad, R.A. Fraser, M. Fowler, Electrochemical modeling of commercial LiFePO4 and graphite electrodes: Kinetic and transport properties and their temperature dependence, J. Electrochem. Soc. 163 (13) (2016) A2803, http://dx.doi.org/10.1149/2.1151613jes.

[89] T. Swamy, Y.-M. Chiang, Electrochemical charge transfer reaction kinetics at the silicon-liquid electrolyte interface, J. Electrochem. Soc. 162 (13) (2015) A7129, http://dx.doi.org/10.1149/2.0181513jes.

[90] J. Schmalstieg, C. Rahe, M. Ecker, D.U. Sauer, Full cell parameterization of a high-power lithium-ion battery for a physico-chemical model: Part I. Physical and electrochemical parameters, J. Electrochem. Soc. 165 (16) (2018) A3799, http://dx.doi.org/10.1149/2.0321816jes.

[91] M. Ecker, T.K.D. Tran, P. Dechent, S. Käbitz, A. Warnecke, D.U. Sauer, Parameterization of a physico-chemical model of a lithium-ion battery: I. Determination of parameters, J. Electrochem. Soc. 162 (2015) A1836–A1848, http://dx.doi.org/10.1149/2.0551509jes].

[92] T.F. Fuller, M. Doyle, J. Newman, Simulation and optimization of the dual lithium ion insertion cell, J. Electrochem. Soc. 141 (1) (1994) 1, http://dx.doi.org/10.1149/1.2054684.

[93] B. Marinho, M. Ghislandi, E. Tkalya, C.E. Koning, G. de With, Electrical conductivity of compacts of graphene, multi-wall carbon nanotubes, carbon black, and graphite powder, Powder Technol. 221 (2012) 351–358, http://dx.doi.org/10.1016/j.powtec.2012.01.024, Selected papers from 2010 AIChE Annual Meeting.

[94] F.L. Vogel, Intercalation compounds of graphite, in: Molecular Metals, Springer US, Boston, MA, 1979, pp. 261–279, http://dx.doi.org/10.1007/978-1-4684-3480-4_27, (Chapter Hatfield, William E.).

[95] G. Mu, B. Wu, C. Ma, F. Wu, Dynamics analysis of Si electrode particle size effect employing accurate Si model, Electrochim. Acta 377 (2021) 138110, http://dx.doi.org/10.1016/j.electacta.2021.138110.

[96] J.H. Ryu, J.W. Kim, Y.-E. Sung, S.M. Oh, Failure modes of silicon powder negative electrode in lithium secondary batteries, Electrochem. Solid-State Lett. 7 (10) (2004) A306, http://dx.doi.org/10.1149/1.1792242.

[97] N. Kirkaldy, M.A. Samieian, G.J. Offer, M. Marinescu, Y. Patel, Lithium-ion battery degradation: Measuring rapid loss of active silicon in silicon–graphite composite electrodes, ACS Appl. Energy Mater. 5 (11) (2022) 13367–13376, http://dx.doi.org/10.1021/acsaem.2c02047.

[98] S. Hein, T. Danner, D. Westhoff, B. Prifling, R. Scurtu, L. Kremer, A. Hoffmann, A. Hilger, M. Osenberg, I. Manke, M. Wohlfahrt-Mehrens, V. Schmidt, A. Latz, Influence of conductive additives and binder on the impedance of lithium-ion battery electrodes: Effect of morphology, J. Electrochem. Soc. 167 (1) (2020) 013546, http://dx.doi.org/10.1149/1945-7111/ab6b1d.